Voltage- and Branch-specific Climbing Fiber Responses in Purkinje Cells

Yunliang Zang[1], Stéphane Dieudonné[2] & Erik De Schutter[1,3*]

[1]Computational Neuroscience Unit, Okinawa Institute of Science and Technology Graduate University, Okinawa 904-0495, Japan

[2]Inhibitory Transmission IBENS, CNRS UMR UMR8197, INSERM U1024, Ecole Normale Supérieure, 75005 Paris, France

[3]Lead Contact

*Correspondence: erik@oist.jp

Summary

Climbing fibers (CFs) provide instructive signals driving cerebellar learning, but mechanisms causing the variable CF responses in Purkinje cells (PCs) are not fully understood. Using a new experimentally validated PC model, we unveil the ionic mechanisms underlying CF-evoked distinct spike waveforms on different parts of the PC. We demonstrate that voltage can gate both the amplitude and the spatial range of CF-evoked Ca^{2+} influx by the availability of K^+ currents. This makes the energy consumed during a complex spike (CS) also voltage-dependent. PC dendrites exhibit inhomogeneous excitability with individual branches as computational units for CF input. The variability of somatic CSs can be explained by voltage state, CF activation phase, and instantaneous CF firing rate. Concurrent clustered synaptic inputs affect CSs by modulating dendritic responses in a spatially precise way. The voltage- and branch-specific CF responses can increase dendritic computational capacity and enable PCs to actively integrate CF signals.

Introduction

According to the Marr-Albus-Ito theory (Albus, 1971; Ito, 1972; Marr, 1969), climbing fiber (CF) inputs to Purkinje cells (PCs) carry movement error information and evoke cerebellar learning by depressing the strength of parallel fiber (PF) synaptic input. Recently, processing of CF-carried error information by PCs has become a focus of cerebellar research (Najafi et al., 2014; Yang and Lisberger, 2014), with increased attention to modifiable dendritic responses (Davie et al., 2008; Kitamura and Hausser, 2011; Najafi et al., 2014; Rokni et al., 2009). Unfortunately, the biophysical mechanisms underlying the voltage-related dendritic response amplitude are still unresolved. CF provides powerful synaptic input onto proximal dendrites, but Ca^{2+} influx in distal dendrites is found to be unreliable (Ohtsuki et al., 2012; Otsu et al., 2014; Zagha et al., 2010). The pattern of dendritic spike initiation and propagation is important because the spatial range of Ca^{2+} influx controls the dendritic sites undergoing synaptic plasticity and even the direction of cerebellar learning. Moreover, whether individual branches of PC dendritic trees are homogeneously excitable has never been investigated due to technical limitations. The effect of clustered PF synaptic input (Wilms and Hausser, 2015) on CF-evoked dendritic responses is also unknown. The answers to these questions will determine whether the computational unit of CF responses is the entire dendritic tree or individual branches.

Somatic complex spikes (CSs) were assumed to be a result of synaptic input current and somatic ionic currents (Schmolesky et al., 2002). Observations that dendritic spike variation plays a minimal role in evoking an extra somatic spikelet seemed to confirm this assumption (Davie et al., 2008), however, contrary observations exist (Ohtsuki et al., 2012; Otsu et al., 2014). Somatic CSs are quite variable (Burroughs et al., 2017;

49 Warnaar et al., 2015) and their durations have been linked with the degree of trial-over-
50 trail learning (Yang and Lisberger, 2014). Voltage states or simple spike firing rates
51 (SSFRs) (well known to represent voltage states *in vitro* and recently demonstrated *in*
52 *vivo* (Jelitai et al., 2016)) have been correlated with CS spikelet numbers in some
53 studies (Burroughs et al., 2017; Gilbert, 1976; Khaliq and Raman, 2005; Monsivais et
54 al., 2005), but not in others (Mano, 1970; Warnaar et al., 2015). Additionally, CSs can
55 be modulated by CF FRs (Hansel and Linden, 2000), but contradictory correlations
56 between spikelet numbers and the instantaneous CF FRs have been reported (Burroughs
57 et al., 2017; Khaliq and Raman, 2005; Maruta et al., 2007; Warnaar et al., 2015). Thus,
58 it is necessary to re-examine how the CS shape is regulated.
59   Spiking is energetically expensive (Attwell and Laughlin, 2001). Each CS consumes
60 more energy than a SS, but neither can be measured experimentally.
61   To address these questions, a systematic exploration of CF responses with high
62 spatio-temporal resolution is required. Given the difficulty of simultaneously recording
63 at numerous locations in the same cell by patch-clamp (Davie et al., 2008; Stuart and
64 Hausser, 1994) and the lack of direct spike information from Ca^{2+} imaging (Deneux et
65 al., 2016), computer models can play an indispensable role. Here we have built a
66 'canonical' PC model that reproduces most available experimental observations instead
67 of fitting it to a specific cell recording. We use this model to systematically explore
68 factors that affect CF-evoked dendritic and somatic responses and estimate the energy
69 consumed for SSs and CSs.

Results

Electrophysiological properties of SSs

72 Before using the model to make predictions, we first compare its basic properties with
73 *in vitro* experimental data. Example cell recordings are shown in Fig. 1A-D to help the
74 comparison. Our PC model spontaneously fires at 40 Hz in the absence of synaptic
75 inputs or current injections (27 to 140 Hz in experiments). SSs initiate first at the axon
76 initial segment (AIS) with an axosomatic delay of 0.12 ms (~ 0.1 ms reported by Palmer
77 et al. (2010)). The SS peak is -1 mV and its amplitude is 68 mV (-11 to -3 mV and 56
78 to 68 mV respectively in experiments). SSs have a half-amplitude duration of 0.22 ms
79 (0.22 to 0.28 ms in experiments). The peak *dv/dt* of SSs is 530 mV/ms (440 to 540
80 mV/ms in experiments). The *d^2v/dt^2* of SSs shows a biphasic increase, with the first
81 component reflecting the contribution of axial current from the AIS and the second one
82 reflecting the contribution of somatic Na^+ current. The peak value of *d^2v/dt^2* is 6600
83 mV/ms^2 (5600 to 8200 mV/ms^2 in experiments).
84   Due to the absence of dendritic Na^+ channels (Stuart and Hausser, 1994) and the
85 large impedance load of elaborate dendritic trees (Vetter et al., 2001), SSs fail to invade
86 the dendritic tree (Llinas and Sugimori, 1980). The distance-dependent decay of SS
87 amplitudes in the model matches experimental data (Fig. 1E; also close to Stuart and
88 Hausser (1994)). The model also performs well in response to somatic current
89 injections. The F-I curve falls within the experimentally measured range (Fig. 1F).
90 Similar with Fernandez et al. (2007), our model has type-I excitability. When a large
91 enough negative current is injected, the cell is silenced and shows a typical 'sag'
92 response (illustrated in the inset of Fig. 1G). Both the peak and steady state of the 'sag'
93 response are within the range of experimental data (Fig. 1G).

2
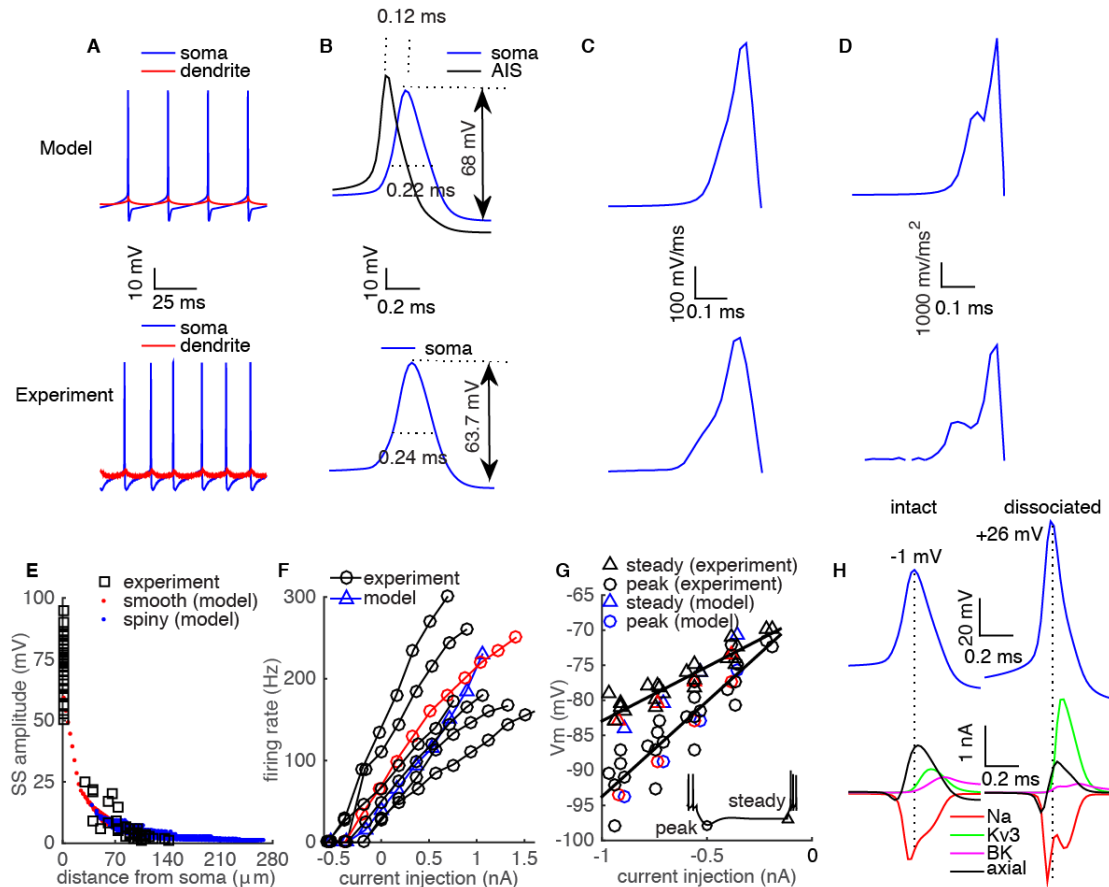
Figure 1. Model properties compare well with experimental data.
A. Spontaneously firing SSs and dendritic membrane potentials (103 μm from soma) from the model and experiments (dendritic site is ~ 100 μm from soma). **B.** A single SS from the model and experiments. The spike at the AIS is aligned to measure the axosomatic delay in the model. The *dv/dt* and *d²v/dt²* of the SS in the model are compared with experimental data in **C** and **D** separately. **E**, Distance-dependent decay of SS amplitudes in the model and experimental data (Ohtsuki et al. (2012)). **F**, The F-I curve of the model compared with experimental data. **G**, The peak and steady state values of 'sag' responses caused by negative current injections are compared between model and experimental data. In F-G, red symbols are from the example cell used in A-D. The data used in A-D, F-G are from Rancz and Hausser (2010). **H**, Distinct spike peaks and principal ionic current profiles in the intact and the dissociated PC model. In the dissociated PC, only the dendritic root section before the first bifurcation is preserved. Ionic currents are computed at the central segment (surface area of 204 μm²) of the soma.

This good overall performance in response to current injections suggests that the model is reliable in predicting excitatory and inhibitory synaptic responses in PCs.

Dissociated PCs are often used to investigate the role of ionic currents in PC electrophysiological properties (Carter and Bean, 2009; Khaliq et al., 2003; Swensen and Bean, 2003). However, we find the profiles of Na⁺ current (principal depolarization current (Carter and Bean, 2009)) and of Kv3 current (principal repolarization current (Martina et al., 2007)) in an intact PC strongly differ from in a dissociated PC owing to their distinct spike properties (Fig. 1H). Similar with Bekkers and Hausser (2007), the intact PC model exhibits a higher spike threshold, smaller afterhyperpolarization and lower spike peak compared with the dissociated PC. The lower spike peak (-1 mV in the model) compared with the dissociated PC (+26 mV in the model, +32 mV in Carter and Bean (2011) and ~ +40 mV in Bekkers and Hausser (2007)) leads to a much smaller fraction of Kv3 channels activated, due to their high activation threshold (Martina et al., 2007). In the intact PC, the dendrite repolarizes somatic SSs together with the 'less' activated Kv3 current. This large axial current (flow into dendrite) keeps pace with SS

3

123   depolarization to constrain its peak to -1 mV (a smaller axial current exists in the
124   dissociated PC due to the remaining dendritic stump). At the peak of the spike, the 'dip'
125   in the Na^+ current observed in dissociated PCs (Carter and Bean, 2009) is absent in the
126   intact PC model.

127   The Na^+ entry ratio (the ratio of total Na^+ influx to the Na^+ influx during the rising
128   phase (Carter and Bean, 2009)) can decrease from 3.0 in the dissociated PC model to
129   2.2 in the intact PC model. Although dendrites lack Na^+ channels, SSs passively
130   propagate into dendrites and partially activate Ca^{2+} channels in proximal dendrites.
131   Therefore, we compute the ATP molecules required for each SS to better understand
132   their energy consumption (Attwell and Laughlin, 2001). In our model, 4.3×10^7 ATP
133   molecules are required to pump Na^+ ions and Ca^{2+} ions out of the PC after a SS, with
134   60% of the energy expended on Na^+ ions.

CF responses in the PC

136   When PCs receive synaptic inputs from CFs, stereotypical CSs occur at their somas.
137   CF responses at different sites of a spontaneously firing PC model are shown in Fig.
138   2A. The peak *dv/dt* of the first spikelet in the CS is ~ 270 mV/ms larger than that of the
139   SS, as confirmed by *in vitro* experimental data (Fig. 2B). The large peak *dv/dt* of the
140   first spikelet ensures its reliable propagation down to the cerebellar nuclei (CN) (Khaliq
141   and Raman, 2005; Monsivais et al., 2005). The CS still initiates first at the AIS (Palmer
142   et al., 2010) with an axosomatic delay of the first spikelet of 0.06 ms, which is much
143   shorter than that of the SS (Fig. 2C). This decreased axosomatic delay is caused by the
144   depolarizing CF EPSC during the initial depolarization phase (Fig. 2D). The model also
145   replicates varied CF responses due to bursting CF input (Mathy et al., 2009) (Fig. S1).

146   In agreement with previous experimental findings (Swensen and Bean, 2003), the
147   SK2 current terminates the CS (Fig. 2D). Each spikelet of the somatic CS in our model,
148   except the last one, is sharp (Fig. 2A), suggesting they are generated by Na^+ channels
149   (Fig. 2D). Two factors determine the absence of Ca^{2+} spikes at the soma. First, the P-
150   type Ca^{2+} current is much smaller than the Na^+ current; therefore, the Na^+ current shunts
151   it. Second, K^+ currents are always larger than the P-type Ca^{2+} current (Fig. 2D).
152   Magnitudes of the CF EPSC and the net axial current are comparable to somatic ionic
153   currents (Fig. 2D), suggesting an important role in generating somatic CSs.
154   Consequently, a variation of either CF EPSC or axial current has the potential to alter
155   somatic CSs, as shown in later sections.

156   The dendritic root section (the section between the soma and the first dendritic
157   bifurcation) is electrically compact with the soma and shows mainly a passive
158   propagation of a somatic CS. With distance from the soma, the clamping effect of the
159   somatic CS on the dendrite weakens. The P-type Ca^{2+} current gradually dominates and
160   cause Ca^{2+}-driven dendritic responses in the PC dendrite (Fig. 2A, E-F).
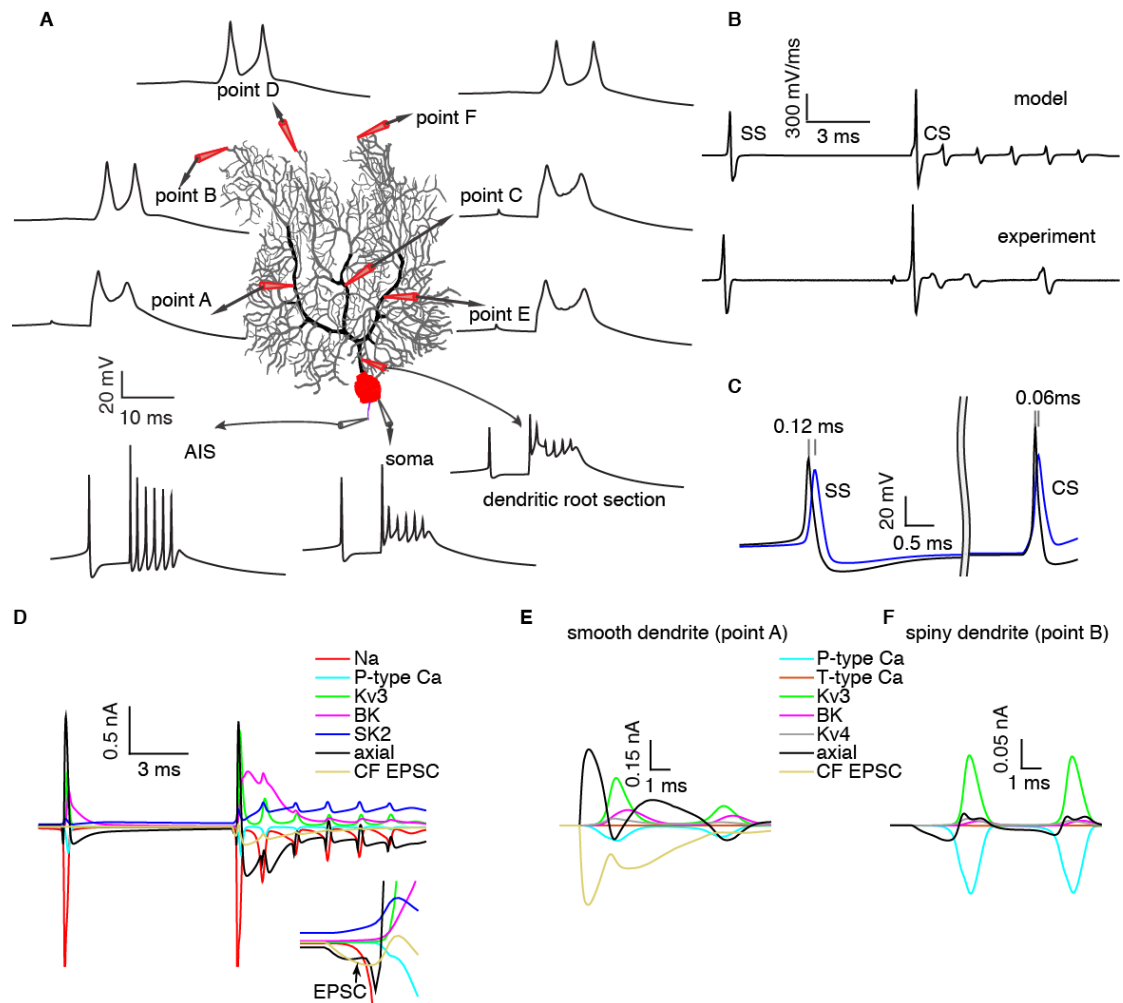
Figure 2. The generation of CF responses in the PC.
A. CF responses at different sites in the PC model. Two sites on each main branch are selected. Points A (smooth dendrite) and B (spiny dendrite) on branch 1; Points C and D on branch 2; Points E and F on branch 3. CF responses at dendritic root section, soma and AIS are labeled by corresponding arrows. **B.** The peak *dv/dt* of the first CS spikelet increases compared with a SS in both model and experiment (Warnaar et al. (2015). **C.** The axosomatic delay of the first spikelet in the CS decreases compared with a SS. **D.** The composition of the somatic CS. Currents at the initial depolarization phase are enlarged in the inset. Dendritic currents at points A and B are shown in **E** and **F** in sequence. The surface areas of the segments chosen at the soma, point A and point B are 204 μm^2, 64 μm^2, and 23 μm^2, respectively. CF EPSC is absent in the spiny dendrite. Notice different scales used in D-F due to different segment surface areas.

Factors regulating the initiation and propagation of dendritic spikes

Here we systematically explore how different voltage states, caused by varying the somatic holding current, regulate CF-evoked dendritic responses and analyze the biophysical mechanisms. We find depolarization facilitates higher peaks of dendritic

5
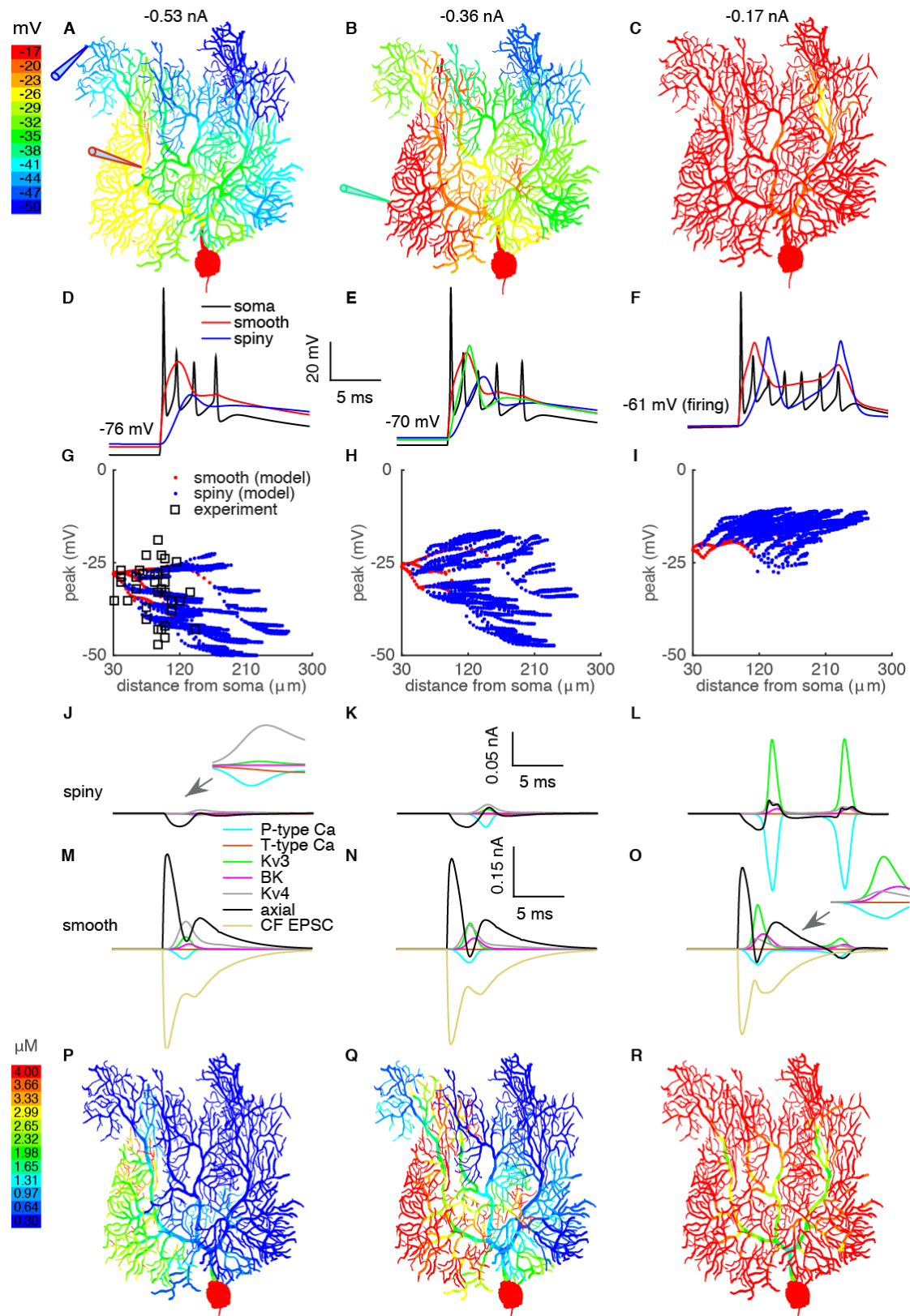
Figure 3. Voltage states regulate CF-evoked dendritic spike generation and propagation. From left to right column, the holding potentials are -76 mV, -70 mV and -60 mV, respectively. **A-C.** Color-coded voltage responses. **D-F.** Somatic CSs, voltage responses on the smooth dendrite and spiny dendrite. In **E**, an extra example voltage response (green trace, position indicated in B) on the spiny dendrite is shown. **G-I.** Distance-dependent propagation of voltage responses. Experimental data in G are from Ohtsuki et al. (2012). **J-L** and **M-O** show ionic currents in the spiny dendrite and smooth

6

185 dendrite respectively. The surface areas of the segments chosen at the smooth dendrite and spiny dendrite
186 are 64 μm^2 and 23 μm^2 respectively. **P-R.** Color-coded Ca^{2+} concentrations.

188 responses with further propagation into distal spiny dendrites. In distal spiny dendrites,
189 axial currents from proximal smooth dendrites are the only current sources that can
190 depolarize to approach the Ca^{2+} spike threshold and trigger a dendritic spike (Fig. 3J-
191 L). When the soma is held at -76 mV (Fig. 3A), the A-type Kv4 current is larger than
192 the P-type Ca^{2+} current in spiny dendrites (Fig. 3J). Consequently, axial currents cause
193 only small passive depolarizations in spiny dendrites (Fig. 3D), and P-type Ca^{2+}
194 channels are hardly activated (Fig. 3J). In smooth dendrites, the CF provides powerful
195 synaptic input to depolarize (Fig. 3D). However, this depolarization is still passive
196 because the Kv4 current and axial currents (flow into distal parts) stop the P-type Ca^{2+}
197 current from dominating depolarization (Fig. 3M). Accordingly, the dendritic voltage
198 responses decrease with distance from the soma in the whole dendrite (Fig. 3G).
199 Distance-dependent propagation of voltage responses matches experimental recordings
200 under the same conditions (Fig. 3G). As the soma is held at -70 mV (Fig. 3B), dendritic
201 spikes occur in part of the dendritic tree (the left half, proximal to the soma), where the
202 voltage responses now increase with distance from the soma. However, the responses
203 still decay with distance from the soma in other parts of the dendritic tree (Fig. 3B,E,H).
204 With depolarization of the soma to -61 mV (Fig. 3C), the Kv4 current gradually
205 inactivates and becomes smaller than the P-type Ca^{2+} current in both smooth and spiny
206 dendrites during the initial depolarization phase (Fig. 3L,O). As a result, the P-type
207 Ca^{2+} current depolarizes the dendrites and activates more Ca^{2+} channels in a positive
208 feedback loop until the Kv3 current is highly activated to repolarize the spikes.
209 Dendritic spikes occur globally and their peaks increase with distance from the soma
210 (Fig. 3F,I). In line with voltage responses, the dendritic Ca^{2+} influx is also facilitated
211 by depolarization, causing larger and more widespread elevations in dendritic Ca^{2+}
212 concentration (Fig. 3P-R). Additional CF responses at other voltage states are shown in
213 Fig. S2.
214 The critical role of Kv4 current in regulating dendritic spike propagation is further
215 demonstrated in Fig. S3. After blocking dendritic Kv4 current, dendritic spikes reliably
216 propagate to the whole dendrite at more hyperpolarized conditions. We further test
217 whether other K^+ currents regulate the propagation of CF-evoked dendritic response.
218 Blocking the high threshold-activated Kv3 current surprisingly facilitates the
219 propagation of dendritic spikes (Fig. S4) (Otsu et al., 2014; Zagha et al., 2010). Unlike
220 the 'brake' mechanism of Kv4 current, dendritic Kv3 current mainly narrows the CF
221 response and only activates when the response is large enough (Fig.3 J-O). Blocking
222 the Kv3 current broadens the dendritic responses at smooth dendrites and facilitates
223 their propagation to spiny dendrites. The effect of broadening dendritic responses on
224 their propagation is further demonstrated in Fig. S5. Dendritic BK current does not
225 significantly affect the propagation of CF-evoked dendritic responses (data not shown).
226 Taken together, these results suggest that availability of dendritic K^+ channels not
227 only regulates the amplitude (Kitamura and Hausser, 2011; Rokni et al., 2009) but also
228 gates the spatial range of Ca^{2+} influx (Ohtsuki et al., 2012; Otsu et al., 2014; Zagha et
229 al., 2010). Voltage conditions can also explain the distinct dendritic spike waveforms
230 recorded *in vitro* by different groups (Davie et al., 2008; Ohtsuki et al., 2012) in Fig.
231 S6.

232 **Inhomogeneous excitability of the dendritic tree**

233 Similar to the first dendritic spikelet (Fig. 3B), the secondary dendritic spikelet occurs
234 asynchronously in different branches around its threshold (Fig. 4). It initially occurs at

235 branch 1; then it gradually occurs at branch 2 and finally occurs at branch 3 with slightly
236 increasing depolarization. Even when secondary dendritic spikelets occur globally,
237 their time to peak still differs between branches (Fig. 4C). They peak at 8.36 ms, 10.74
238 ms and 13.64 ms at points A, C and E respectively (relative to CF activation time). With
239 further depolarization, secondary dendritic spikelets peak more synchronously (with
240 0.89 nA current injection, the respective values become 6.06 ms, 6.88 ms and 7.32 ms).
241 The asynchronous occurrence of individual spikelets reflects the inhomogeneous
242 excitability of each dendritic branch. In the model, the density of ionic currents is
243 homogeneous in the spiny dendritic tree. Therefore, morphological differences between
244 individual branches may account for heterogeneous excitability. The excitability of
245 each branch is determined by the ratio of spiny dendrite area to smooth dendrite length
246 in that branch (essentially the ratio of spiny dendrite capacitance load to CF synaptic
247 input, 'load/input' ratio, see Methods). The 'load/input' ratios are 69, 96 and 130 at
248 branches 1, 2 and 3 respectively, explaining their heterogeneous excitability. Moreover,
249 within each 'big' branch, 'small' child branchlets also show heterogeneity
250
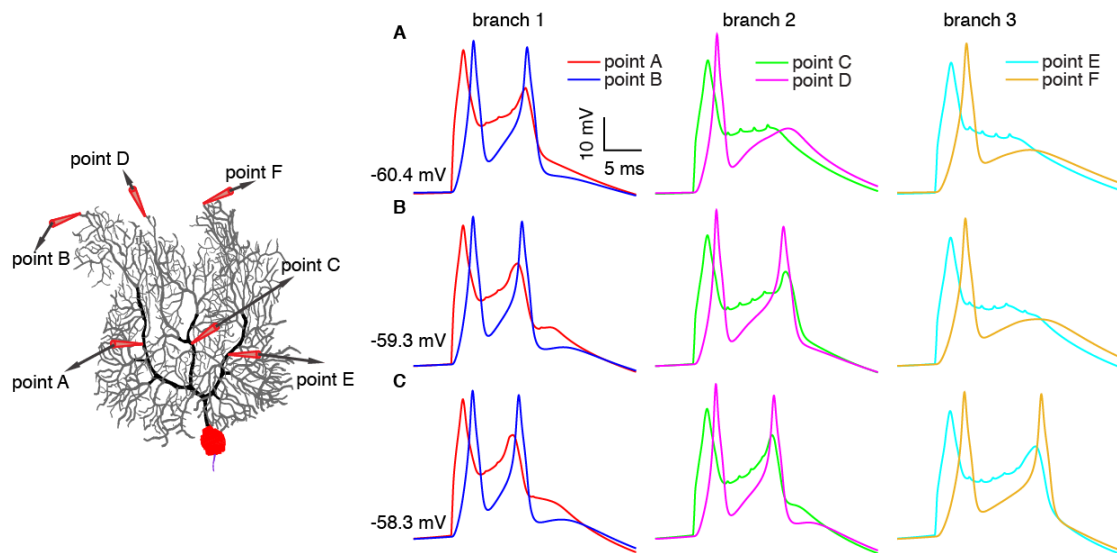
253 **Figure 4. Branch-specific occurrence of secondary dendritic spikelets.**
254 In all simulations, the holding current is -0.17 nA. CF input is activated at three slightly different dendritic
255 voltage states (different phases of somatic interspike intervals) as shown in **A**, **B**, and **C**.

257 in excitability (Fig. 3A-C), which are caused by other morphological factors such as
258 the electrotonic distance to smooth dendrites.
259   K^+ currents activated near 'resting' dendritic membrane potentials may enhance the
260 heterogeneous excitability. The whole dendrite becomes more homogeneous at
261 hyperpolarized levels after blocking the Kv4 current (Fig. S3). Essentially, uneven
262 distributed 'load/input' ratios underlie the heterogeneous dendritic excitability, but
263 dendritic Kv4 channels enhance it.

Voltage- and phase-dependent somatic CSs
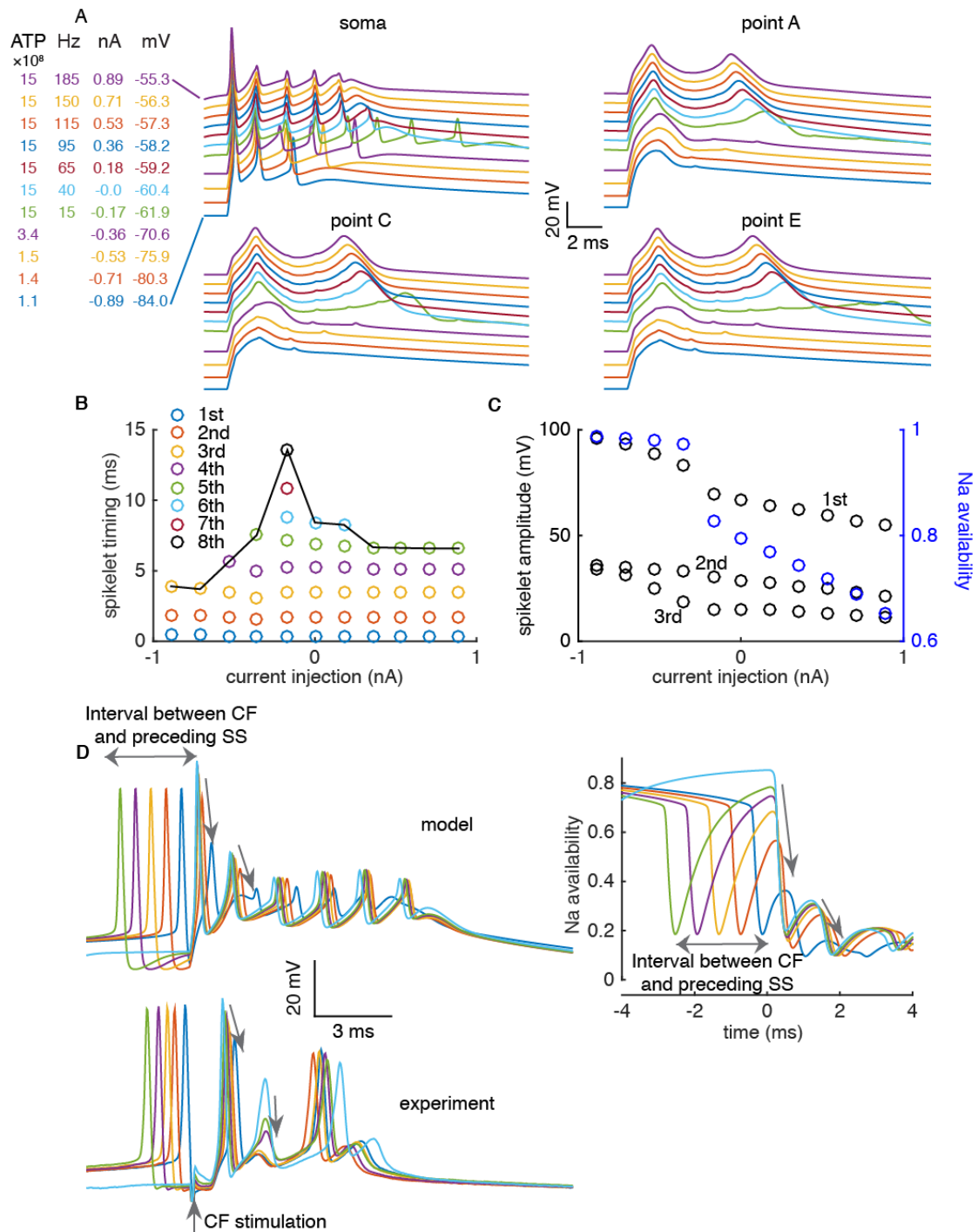
Figure 5. Voltage- and phase-dependent somatic CSs.
A. Voltage states affect somatic CSs and corresponding dendritic responses. The definition of dendritic sites is the same as in Fig. 2. The holding currents, the FRs and the consumed ATP molecules at each voltage state are listed on the left. **B.** Voltage states modulate CS durations, represented by the timing of the last spikelets. **C.** In parallel with Na^+ channels availability (blue circles), amplitudes of the first three spikelets in the CS (black circles) decrease with depolarization. **D.** Amplitudes of the first and second spikelets are phase-dependent in model and experiments (Warnaar et al. (2015)). Phase-dependent recovery of Na^+ channels is shown in upper right panel.

Similar with dendritic responses, somatic CSs also vary significantly with depolarization (Fig. 5A-C). The spikelet numbers in CSs increase with initial depolarization, but decrease with further depolarization. A somatic CS results from the

277 interaction of intrinsic ionic currents, axial current, and CF EPSC (Fig. 2D). At low
278 voltage, although Na$^+$ channel availability decreases slightly (Fig. 5C), increased axial
279 current from larger dendritic responses (Fig. 5A) dominates and triggers more somatic
280 spikelets. Interestingly, the largest number of somatic spikelets coincides with the
281 longest occurrence latency of secondary dendritic spikelets (Fig. 5A). With further
282 depolarization, Na$^+$ channel availability decreases at a higher rate (Fig. 5C). Also,
283 secondary dendritic spikelets peak faster and closer to a preceding somatic spikelet (Fig.
284 5A). The shortened interval between secondary dendritic spikelets and their preceding
285 somatic spikelet means fewer Na$^+$ channels are recovered to evoke an extra somatic
286 spikelet (right axis of Fig. 5D). The critical role of secondary dendritic spikelet timing
287 in evoking an extra somatic spikelet agrees with previous experimental observations
288 (Davie et al., 2008). Both factors decrease somatic spikelets with further depolarization.
289 Concurrent with spikelet numbers, CS durations are regulated by voltage states, as
290 represented by the timing of the last spikelets (Fig. 5B).

291 With depolarization, the consumed ATP molecules during CSs increase from
292 1.1×10^8 (-84 mV) to 1.5×10^9 for a CS with two dendritic spikelets (nearly 40 times as
293 large as in a SS), with 96% of the energy expended on Ca^{2+} ions (Fig.5A). The increased
294 ATP consumption with depolarization is due to increased Ca^{2+} influx (Fig. 3,5A,S2),
295 but relatively insensitive to somatic spikelet variations.

296 Voltage states also affect spikelet amplitudes in CSs. We analyzed the first three
297 spikelets, which exist in all simulated voltage conditions. Spikelet amplitudes decrease
298 with depolarization due to reduced availability of Na$^+$ channels (Fig. 5C). Individual
299 spikelet amplitude is critical because it determines the probability of propagation down
300 to the CN (Khaliq and Raman, 2005; Monsivais et al., 2005).

301 Finally, we observed phase-dependency of somatic CSs. Amplitudes of the first two
302 spikelets in CSs decrease and the spikelets become more blunted with shortening of the
303 interval between the CF activation and its preceding SS (Fig. 5D). This phase-
304 dependency reflects the time course of Na$^+$ channel recovery from inactivation. We
305 confirmed this phase-dependency by reanalyzing *in vitro* experimental recordings.

306 So far, voltage states of the PC model were manipulated by varying somatic holding
307 currents. We implemented more realistic *in vivo* simulations (Jelitai et al., 2016), in
308 which the net balance of excitatory PF and inhibitory synaptic inputs determines the
309 dendritic voltage states (Fig. S7). We find that the effect of voltage states on CF
310 responses found *in vitro* also holds *in vivo*. We also analyze pauses following CSs (data
311 *in vitro* not shown) and find their durations decrease with depolarization in our model
312 (Fig. S7I), due to the larger depolarization force.

313 Spatially constrained modulation by clustered PF/stellate cell synaptic input

314 Sensory stimuli can activate clustered PF synaptic inputs (Wilms and Hausser, 2015).
315 Here we examine how simultaneous clustered PF or stellate cell synaptic inputs regulate
316 CF responses. We find that clustered synaptic inputs regulate dendritic responses in a
317 spatially constrained manner. A secondary dendritic spikelet only occurs at branch 1
318 with CF input in isolation (Fig. 6A). With 5 PF synapses simultaneously activated at
319 the indicated branchlet of branch 2, the secondary dendritic spikelet also occurs at this
320 branchlet. Concurrently, an extra spikelet is evoked in the somatic CS. Nonetheless,
321 clustered PF synaptic inputs within branch 2 don't significantly affect other branches.
322 Seemingly paradoxically, the extra somatic spikelet is eliminated if the number of
323 simultaneously activated PF synapses increases to 20. As explained previously, Na$^+$
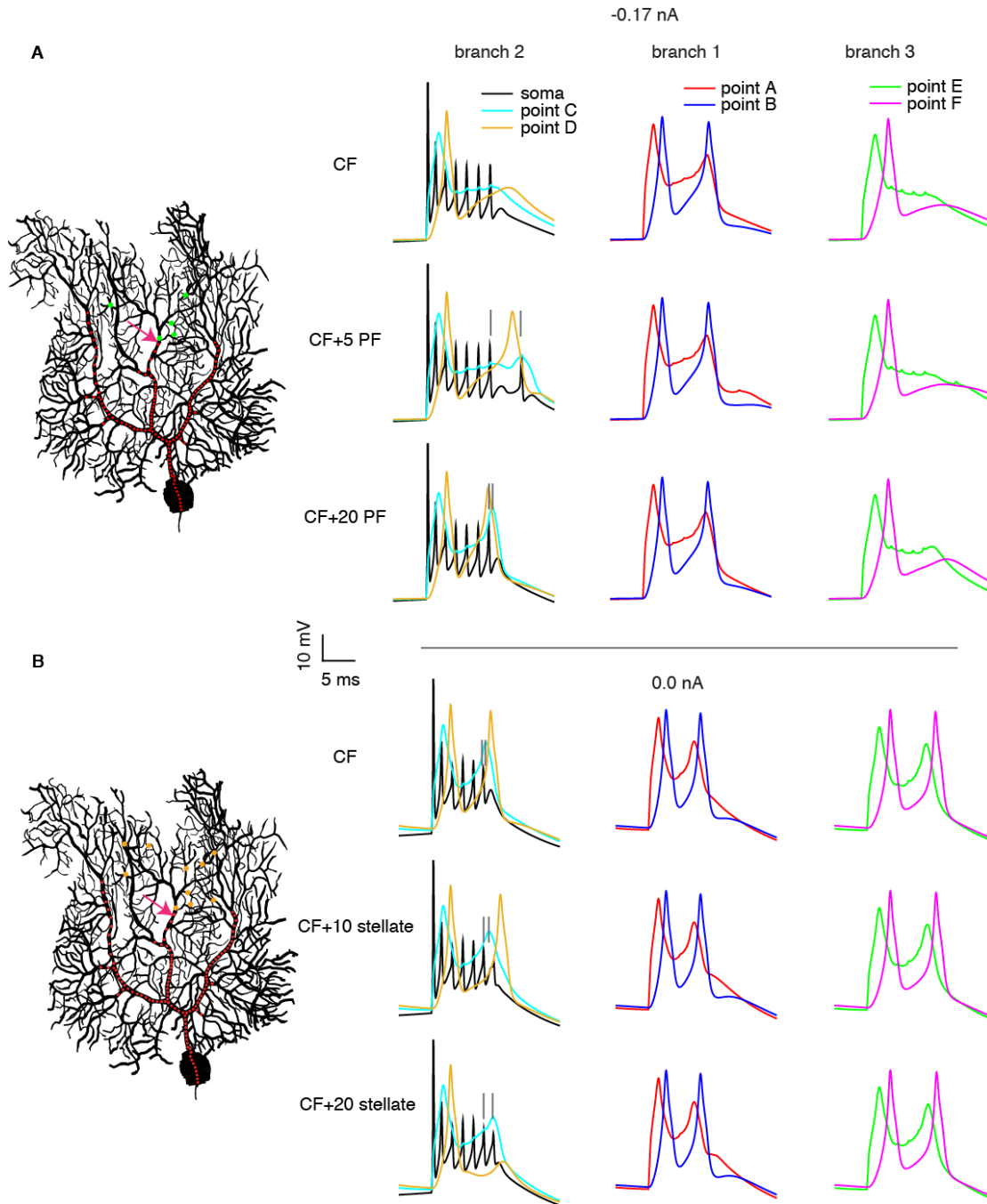324 channels need time to recover from inactivation after each
325

Figure 6. Simultaneous clustered PF or stellate cell synaptic input regulates the CF-evoked somatic CSs by locally modulating the dendritic responses.
A. Somatic and dendritic responses with only CF input (red dots), CF input + 5 PF synaptic inputs and CF input + 20 PF synaptic inputs are shown from top to bottom. PF synapses are randomly distributed on the child branchlet of the indicated dendritic section (green dots). **B.** Somatic and dendritic responses with only CF input, CF input + 10 stellate cell synaptic inputs and CF input + 20 stellate cell synaptic inputs are shown from top to bottom. Similar placement of stellate cell synapses (orange dots). The definition of recorded dendritic sites is the same as in Fig. 2.

somatic spikelet. Increasing PF synaptic inputs accelerates secondary dendritic spikelets, making them occur closer to the preceding somatic spikelet, and reducing the likelihood of triggering an extra spikelet due to fewer recovered Na$^+$ channels. Similarly, simultaneous activation of 10 stellate cell synaptic inputs can evoke an extra somatic spikelet by delaying the secondary dendritic spikelets at branch 2 (Fig. 6B).

11

342   Again, dendritic responses at other branches are minimally affected. The secondary
343   dendritic spikelet still occurs in the proximal smooth dendrite even when it is eliminated
344   in the distal part by activating 20 stellate cell synaptic inputs.
345   We also show that compartment-specific dendritic excitability (Ohtsuki et al., 2012),
346   simulated here by regional Kv4 block, modulates dendritic responses in a spatially
347   precise way (Fig. S8).

348   **Paired-pulse depression regulates CF responses in the PC**
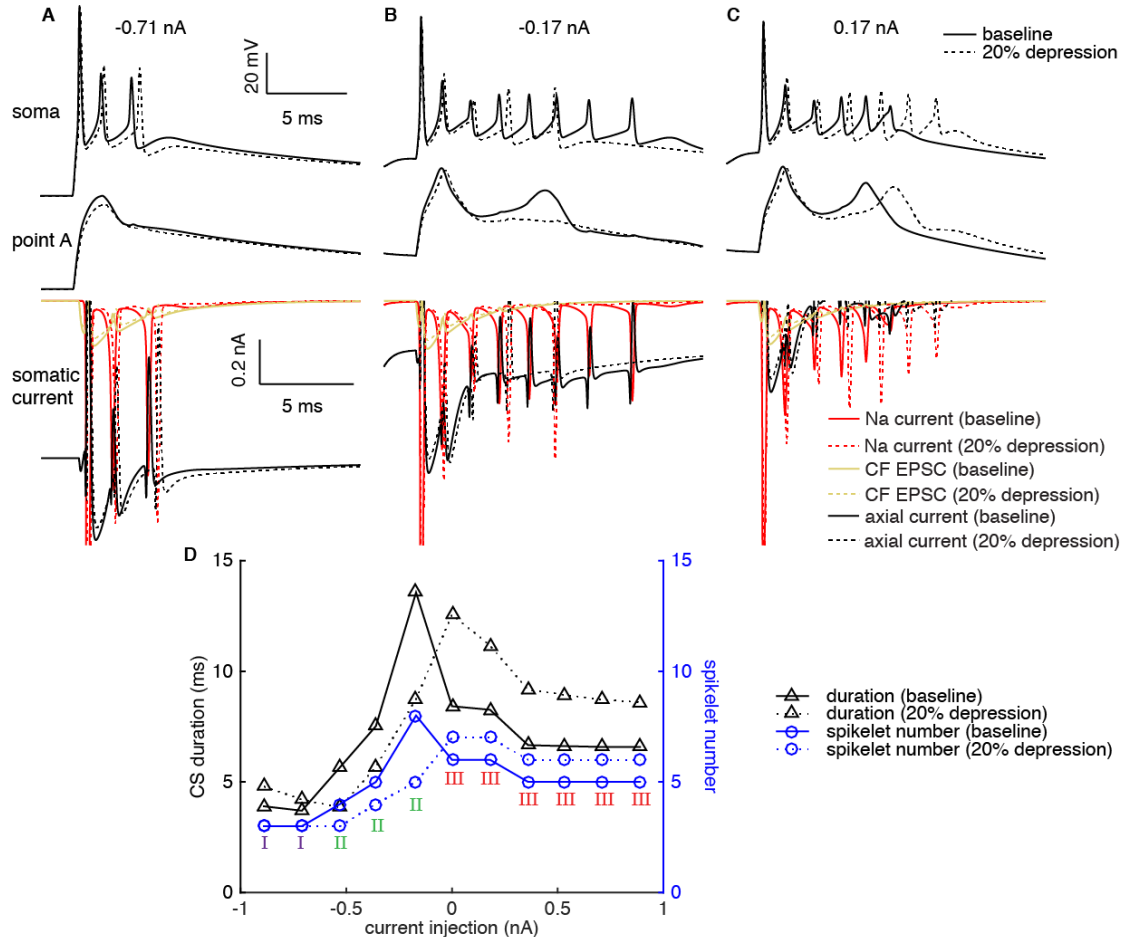
349
350 **Figure 7. PPD regulates CF responses.**
351 CF responses (somatic and dendritic) and somatic ionic currents with unchanged (case I), decreased (case
352 II) and increased (case III) spikelet numbers per CS by depressed CF EPSC are shown in **A**, **B** and **C** in
353 sequence. Ionic currents are computed in the central segment of the soma and Na$^+$ currents during the
354 first spikelet are truncated. **D**. The effect of depressed CF EPSC on the spikelet number and duration of
355 the CSs.
356

357   CFs can transiently fire at ~ 5 - 8 Hz after sensory stimuli (Najafi et al., 2014; Warnaar
358   et al., 2015). Paired-pulse depression (PPD) has been demonstrated for consecutive CF
359   synaptic inputs *in vitro* (Andjus et al., 2005; Hansel and Linden, 2000) and it may
360   support the correlation between instantaneous CF FRs and varied CS spikelet numbers.
361   To investigate the effect of PPD on CF responses, we systematically explore CF
362   responses with baseline or 20% depressed CF EPSC (~ 4 Hz of instantaneous CF FR
363   in experiments by Andjus et al. (2005)). We find depressed CF inputs consistently
364   reduce dendritic responses. At low voltage, the peak of the dendritic response decreases
365   (Fig. 7A); at higher voltage, the appearance of a secondary dendritic spikelet is
366   prevented (Fig. 7B) or delayed (Fig. 7C). The spikelet numbers in somatic CSs show
367   no changes, decreases or increases with depressed CF inputs at different voltages (Fig.

7A-C). A depressed CF input always delays individual somatic spikelets by providing less depolarization current. At low voltage, 20% depression of the CF EPSC and slightly reduced dendritic response are insufficient to vary somatic spikelet number and only increase CS duration (Fig. 7A and Case I in Fig. 7D). At medium voltage, baseline CF input evokes a secondary dendritic spikelet. The increased axial current (the later stage of ionic currents in Fig. 7B) triggers extra somatic spikelets due to the relatively large availability of Na^+ channels (see Na^+ current amplitude). Therefore, by not causing a secondary dendritic spikelet, depressed CF input decreases CS duration because of fewer somatic spikelets, although they are delayed (Fig. 7B and Case II in Fig. 7D). At high voltage, depressed CF input delays individual spikelets and allows for larger recovery of Na^+ channels. The delayed secondary dendritic spikelet also facilitates occurrence of extra somatic spikelets. Thus, depressed CF input increases CS duration (Fig. 7C and case III in Fig. 7D).

Voltage ranges for the occurrence of cases I-III depend on the degree of depression. For example, when CF EPSC is depressed by 10%, case I can occur at both low and high voltages (data not shown). Also, when CF FRs are higher, incomplete recovery of ionic currents from preceding CS such as SK2 and the dendritic hyperpolarization may vary the posterior CS in a more complicated way.

PPD can bridge the gap between instantaneous CF FRs and CS variations. Our results reconcile the observed unchanged (Warnaar et al., 2015), decreased (Khaliq and Raman, 2005; Maruta et al., 2007), and increased (Burroughs et al., 2017) somatic spikelet numbers at higher CF FRs.

Discussion

We built a new PC model based on extensive experimental data to systematically investigate CF responses. Simulation results help to reveal the mechanisms causing spikes on different parts of PCs, reconcile conflicting experimental data and make new predictions.

Model accuracy

We constrained model parameters by hand tuning and tried to replicate as many experimental observations as possible. We started by constraining somatic ionic currents based on ionic current measurements taken from dissociated PCs. These data allowed us to uniquely constrain principal somatic currents. Subsequently, the ionic currents in the AIS and dendrites were constrained to obtain the spike properties summarized in Fig. 1. It was more difficult to constrain dendritic ionic currents due to insufficient data. The total Ca^{2+} influx during one dendritic spikelet was constrained by the experimentally estimated value. In addition, the replicated CF-evoked dendritic responses under different conditions (Fig. 3,S2,S4,S6) suggest that the dendrite model produces realistic results. Nonetheless, there is still room for improvement in the future. Due to the lack of specific data, we did not try to reproduce the role of dendritic SK2 current (Ohtsuki et al., 2012; Womack and Khodakhah, 2003) and Kv1 current (Khavandgar et al., 2005) in regulating dendritic excitability. These currents may further enhance the heterogenous excitability and regulate dendritic responses. The data we used to directly validate our simulation results are all from *in vitro*. We hope our study will inspire experiments to validate modifiable CF responses *in vivo*.

Our PC model follows the tradition of the biophysical modeling by De Schutter and Bower (1994a, 1994b), which has successfully predicted experimental findings (Steuber et al., 2007). Although the 1994 model is outdated by recent knowledge of ionic channels in PCs, there was no suitable replacement until now. A PC model by

13

416 Khaliq et al. (2003) has no dendrite and therefore can't be used to simulate synaptic
417 responses. A recent PC model (Masoli et al., 2015) lacks extensive validation against
418 experimental data. For example, it fails to produce the stereotypical 'sag' responses to
419 hyperpolarization.

Physiological predictions and implications

421 The model allows us to predict the metabolic cost of spiking in PCs. In a cortical
422 pyramidal neuron, $\sim 4\times10^8$ ATP molecules are consumed to restore the Na^+ and K^+ ion
423 gradients after each spike (Attwell and Laughlin, 2001). Carter and Bean (2009)
424 reported that spiking is energetically less efficient in PCs compared with cortical
425 pyramidal neurons. However, their study was performed in dissociated PCs. We find
426 the intact PC has a smaller Na^+ entry ratio compared with the dissociated PC (Fig. 1H),
427 suggesting that dendrites increase the metabolic efficiency of somatic spikes. Given the
428 energetic cost of spikes, it will be interesting to explore whether this dendritic role also
429 applies to other neurons. Compared with Na^+ entry ratio, the estimated energy
430 consumption may be a better measure because of the Ca^{2+} channels distributed in soma,
431 axon and elaborate dendritic tree. Interestingly, although cortical pyramidal neurons
432 have a low Na^+ entry ratio (~ 1.1 by Carter and Bean (2009)), their estimated energetic
433 cost of a single spike is ~ 8 times larger than a SS in PCs, due to the lack of Na^+ channels
434 in PC dendrites. Each CS consumes more ATP molecules, which consumes nearly the
435 same amount of energy as 40 SSs during 1 sec in our model. Possibly, previously
436 reported negative correlation (Cerminara and Rawson, 2004) between the FRs of SSs
437 and CSs may be a protective mechanism given the limited energy supply in the
438 cerebellum.

439 CF-evoked dendritic spikes and somatic CSs are generated by different channels
440 intrinsically, but they communicate via axial currents through the dendritic root section
441 (Fig. 2). Due to technical challenges, dendritic patch-clamp recording is usually
442 performed on smooth dendrites of large diameter. Though we could reproduce the
443 experiment by Davie et al. (2008) in the model (Fig. S9), we show that a single-site
444 dendritic recording can't reliably reflect spike occurrence and propagation in the whole
445 dendrite. Both the peak and occurrence latency of secondary dendritic spikelets can be
446 modulated. The peak of secondary dendritic spikelets decreases in the somatopetal
447 direction due to unevenly distributed impedances (Roth and Hausser, 2001; Vetter et
448 al., 2001) and K^+ channels (Martina et al., 2003). When a secondary dendritic spikelet
449 is 'weak', with small amplitude and long latency, it may fail to trigger a regenerative
450 dendritic spike in proximal dendrites (branch 1 in Fig. S9). Therefore the role of
451 dendritic spikes in evoking extra somatic spikelets may have been underestimated.

452 Using the model, we deciphered how voltage-dependent K^+ currents regulate the
453 amplitude (Kitamura and Hausser, 2011; Rokni et al., 2009) and spatial range of Ca^{2+}
454 influx (Fig. 3,S2-S4,S7) as observed in separate experiments (Ohtsuki et al., 2012; Otsu
455 et al., 2014; Zagha et al., 2010). Vetter et al. (2001) have explored the local propagation
456 of dendritic spikes by exerting an AP clamp at a specific dendritic site. We find that
457 dendritic spikes on the smooth dendrite can overcome the impedance mismatch and
458 propagate to distal dendrites in the absence of the 'brake' role of Kv4 in distal dendrites
459 (Fig. S3,S5). Therefore, K^+ currents activated around the 'resting' dendritic membrane
460 potential such as Kv4 in spiny dendrites are necessary to gate the spatial range of CF-
461 evoked dendritic responses. Unlike Kv4 current, Kv3 current narrows the dendritic
462 response to regulate its propagation (Fig. S4,S5). The voltage-related amplitude and
463 spatial range of dendritic responses indicate that PCs can play active roles in response
464 to CF error signals rather than passively accepting instruction from their CF 'teachers'.

14

465   PF synapses can undergo not only LTD (with a higher Ca^{2+}-induction threshold), but
466   also long-term potentiation (LTP, with a lower Ca^{2+}-induction threshold) (Coesmans et
467   al., 2004; Gallimore et al., 2018; Piochon et al., 2016). The voltage-regulated dendritic
468   spike amplitude and spatial range suggest that CF may trigger LTP, a mixture of
469   regional LTP and LTD, or LTD depending on the voltage states of PCs. Such effects
470   will be further modified by stochastic gating of Ca^{2+} and K^+ channels (Anwar et al.,
471   2013), which was not simulated in this study.
472   The PC dendritic tree exhibits inhomogeneous excitability in individual branches,
473   implying a computational unit at the level of individual branches, or even smaller
474   branchlets (Fig. 4). Building upon the modulated voltage states of PCs, branch-specific
475   computation can undoubtedly increase the capacity of information processing in PC
476   dendrites, in contrast to the traditional view of the whole dendrite as the computational
477   unit of CF response. Notably, branchlet-specific Ca^{2+} influx has been demonstrated for
478   PF synaptic integration (Wang et al., 2000). When PCs receive concurrent clustered
479   synaptic input (Wilms and Hausser, 2015) or undergo localized dendritic excitability
480   plasticity (Ohtsuki et al., 2012), CF-evoked dendritic responses can be modulated more
481   precisely in space and magnitude to affect the plasticity induction (Fig. 6,S8).
482   CS shapes are quite variable. In our model, we did not get the 'small' second
483   spikelets as observed in some experiments (Davie et al., 2008; Monsivais et al., 2005),
484   but our CS shapes are close to other recordings (Jelitai et al., 2016; Mathy et al., 2009;
485   Otsu et al., 2014). We speculate that CS shapes are cell-dependent. Recently, CS
486   durations have been linked to the degree of trial-over-trial learning (Yang and Lisberger,
487   2014), with the mechanism underlying variable CSs unresolved. The authors assumed
488   that the variation of CS durations is due to the bursting of CF inputs, based on Mathy
489   et al. (2009). We correlate the spikelet numbers and durations of CSs with voltage states
490   or SSFRs (Fig. 5A-B). Besides reconciling previous contradictory correlations between
491   spikelet numbers and SSFRs (Burroughs et al., 2017; Gilbert, 1976; Khaliq and Raman,
492   2005; Mano, 1970; Warnaar et al., 2015), our results provide an alternative
493   interpretation of the work by Yang and Lisberger (2014). Our interpretation highlights
494   the importance of all synaptic inputs to the PCs and resulting SSFRs, not just CF, to
495   control learning. Additionally, the CS spikelet amplitudes can be modulated by voltage
496   states (Fig. 5C, S7H). The timing of CF activation (phase-dependency) and concurrent
497   synaptic input also affect somatic CSs (Fig. 5D, 6). All these factors vary CS shapes
498   and may modulate the PC output and affect inhibition of the CN. Although CF-evoked
499   pause decreases at higher firing rates (Fig. S7I), they are very variable (Mathy et al.,
500   2009) when voltage states, CF activation phase or CF input conductance are varied.
501   Sometimes, there is even no 'obvious' pause following a CS.
502   The CF input itself is not 'all-or-none' either. The variable number of spikes per CF
503   burst can affect both somatic and dendritic responses (Mathy et al., 2009) (Fig. S1).
504   Furthermore, CF synaptic inputs can be regulated by PPD (Andjus et al., 2005; Hansel
505   and Linden, 2000) and by norepinephrine (Carey and Regehr, 2009). Both of them can
506   depress the CF EPSC to modulate somatic and dendritic responses (Fig.7). In particular,
507   PPD bridges the gap between instantaneous CF FRs and varied CS spikelet numbers
508   (Burroughs et al., 2017; Khaliq and Raman, 2005; Maruta et al., 2007; Warnaar et al.,
509   2015) and can play an important role in regulating CF responses.

510   **Methods**

511   All simulations were performed with NEURON, version 7.4 (Hines and Carnevale,
512   1997). We use the morphology of a 21-day-old Wistar rat PC (Roth and Hausser, 2001).
513   As shown in Fig. 2A, the model consists of an AIS (purple), a soma (red), smooth

15

514 dendrites (black), and spiny dendrites (gray). The first 17 μm of the reconstructed axon
515 are preserved as the AIS. When exploring the spike initiation site, AIS indicates the end
516 next to the myelinated axon. The model has following passive parameters: R_m = 120.2
517 kΩ cm^2, R_i = 120 Ω cm, C_m = 0.64 μF/cm^2. To compensate for the absence of spines in
518 the reconstructed morphology, the conductance of passive current and C_m are scaled by
519 a factor of 5.3 in the spiny dendrite and 1.2 in the smooth dendrite. The conductance
520 densities of ionic currents in different parts of the model were found by hand tuning.
521 Detailed information about ionic current equations and the process of parameter tuning
522 can be found in Supplementary Information.
523 The spiking threshold of SSs was defined as the membrane potential at which dv/dt =
524 20 mV/ms. The synaptic conductance activated by CF input is approximated as a bi-
525 exponential waveform, with 0.3 ms and 3 ms as the rise and decay time constants (Davie
526 et al., 2008). The peak conductance of baseline CF input is 1.2 nS. 500 synaptic inputs
527 are distributed on the soma and smooth dendrite at a constant density per length to
528 simulate the CF input. The conductance varies in the range of 80% - 100% to simulate
529 the EPSC changes by PPD. Due to the elaborate structure, the dendrite is not
530 isopotential with the soma when holding current is injected at the soma. The somatic
531 membrane potential is used to represent the voltage state of the PC except in Fig. 4, in
532 which dendritic membrane potential is used. When measuring the distance-dependence
533 of the peak dendritic response, we selected the first dendritic spikelet if there were two
534 spikelets. To measure the excitability of individual branches, we define a new measure
535 as the ratio of the spiny dendrite capacitance load to CF synaptic input, 'load/input'
536 ratio, which can be transformed into 'area of spiny dendrite'/'length of smooth dendrite'
537 within each branch in the model. To exclude the effect of phase-dependence on CSs in
538 Fig. 5, all the CF signals are activated with 3 ms after the preceding SS under different
539 voltage states. To explore how simultaneous clustered synaptic inputs regulate dendritic
540 response and somatic output, PF or stellate cell synaptic inputs are activated 5 ms after
541 the CF input (Fig. 6). To simply mimic the PC voltage states *in vivo*, 1105 PF synapses
542 and 1105 Inhibitory synapses are uniformly distributed on the spiny dendrites. Different
543 voltage states of the PC are achieved by randomly activating excitatory and inhibitory
544 synapses at different average FRs. To estimate the energy cost of spikes, we computed
545 the Na^+ (3 Na^+ ions consume 1 ATP molecule) and Ca^{2+} influx (1 Ca^{2+} ion consumes 1
546 ATP molecule) during a spike in the whole PC (AIS, soma and dendrite) (Attwell and
547 Laughlin, 2001).

548 **Data availability**. The model code will be available from ModelDB.

549 **Acknowledgements**

556 **Author Contributions**

557 Y.L.Z., S.D., and E.D.S. conceived this study; Y.L.Z. performed all the simulations;
558 Y.L.Z. and E.D.S. analyzed the simulation data; Y.L.Z. and E.D.S. wrote and revised
559 the manuscript.
560

References

Albus, J.S. (1971). A theory of cerebellar function. Mathematical Biosciences *10*, 25-61.

Andjus, P.R., Bajic, A., Zhu, L., Schachner, M., and Strata, P. (2005). Short-term facilitation and depression in the cerebellum: some observations on wild-type and mutant rodents deficient in the extracellular matrix molecule tenascin C. Annals of the New York Academy of Sciences *1048*, 185-197.

Anwar, H., Hepburn, I., Nedelescu, H., Chen, W., and De Schutter, E. (2013). Stochastic calcium mechanisms cause dendritic calcium spike variability. The Journal of neuroscience : the official journal of the Society for Neuroscience *33*, 15848-15867.

Attwell, D., and Laughlin, S.B. (2001). An energy budget for signaling in the grey matter of the brain. Journal of cerebral blood flow and metabolism : official journal of the International Society of Cerebral Blood Flow and Metabolism *21*, 1133-1145.

Bekkers, J.M., and Hausser, M. (2007). Targeted dendrotomy reveals active and passive contributions of the dendritic tree to synaptic integration and neuronal output. Proceedings of the National Academy of Sciences of the United States of America *104*, 11447-11452.

Burroughs, A., Wise, A.K., Xiao, J.Q., Houghton, C., Tang, T.Y., Suh, C.Y., Lang, E.J., Apps, R., and Cerminara, N.L. (2017). The dynamic relationship between cerebellar Purkinje cell simple spikes and the spikelet number of complex spikes. J Physiol-London *595*, 283-299.

Carey, M.R., and Regehr, W.G. (2009). Noradrenergic control of associative synaptic plasticity by selective modulation of instructive signals. Neuron *62*, 112-122.

Carter, B.C., and Bean, B.P. (2009). Sodium entry during action potentials of mammalian neurons: incomplete inactivation and reduced metabolic efficiency in fast-spiking neurons. Neuron *64*, 898-909.

Carter, B.C., and Bean, B.P. (2011). Incomplete inactivation and rapid recovery of voltage-dependent sodium channels during high-frequency firing in cerebellar Purkinje neurons. Journal of neurophysiology *105*, 860-871.

Cerminara, N.L., and Rawson, J.A. (2004). Evidence that climbing fibers control an intrinsic spike generator in cerebellar Purkinje cells. Journal of Neuroscience *24*, 4510-4517.

Coesmans, M., Weber, J.T., De Zeeuw, C.I., and Hansel, C. (2004). Bidirectional parallel fiber plasticity in the cerebellum under climbing fiber control. Neuron *44*, 691-700.

Davie, J.T., Clark, B.A., and Hausser, M. (2008). The origin of the complex spike in cerebellar Purkinje cells. The Journal of neuroscience : the official journal of the Society for Neuroscience *28*, 7599-7609.

De Schutter, E., and Bower, J.M. (1994a). An active membrane model of the cerebellar Purkinje cell II. Simulation of synaptic responses. Journal of neurophysiology *71*, 401-419.

De Schutter, E., and Bower, J.M. (1994b). An active membrane model of the cerebellar Purkinje cell. I. Simulation of current clamps in slice. Journal of neurophysiology *71*, 375-400.

Deneux, T., Kaszas, A., Szalay, G., Katona, G., Lakner, T., Grinvald, A., Rozsa, B., and Vanzetta, I. (2016). Accurate spike estimation from noisy calcium signals for

609   ultrafast three-dimensional imaging of large neuronal populations in vivo. Nature
610   communications *7*, 12190.

611   Fernandez, F.R., Engbers, J.D., and Turner, R.W. (2007). Firing dynamics of
612   cerebellar purkinje cells. Journal of neurophysiology *98*, 278-294.

613   Gallimore, A.R., Kim, T., Tanaka-Yamamoto, K., and De Schutter, E. (2018).
614   Switching On Depression and Potentiation in the Cerebellum. Cell reports *22*, 722-
615   733.

616   Gilbert, P.F. (1976). Simple spike frequency and the number of secondary spikes
617   in the complex spike of the cerebellar Purkinje cell. Brain research *114*, 334-338.

618   Hansel, C., and Linden, D.J. (2000). Long-term depression of the cerebellar
619   climbing fiber--Purkinje neuron synapse. Neuron *26*, 473-482.

620   Hines, M.L., and Carnevale, N.T. (1997). The NEURON simulation environment.
621   Neural computation *9*, 1179-1209.

622   Ito, M. (1972). Neural design of the cerebellar motor control system. Brain
623   research *40*, 81-84.

624   Jelitai, M., Puggioni, P., Ishikawa, T., Rinaldi, A., and Duguid, I. (2016). Dendritic
625   excitation-inhibition balance shapes cerebellar output during motor behaviour.
626   Nature communications *7*, 13722.

627   Khaliq, Z.M., Gouwens, N.W., and Raman, I.M. (2003). The contribution of
628   resurgent sodium current to high-frequency firing in Purkinje neurons: an
629   experimental and modeling study. The Journal of neuroscience : the official journal
630   of the Society for Neuroscience *23*, 4899-4912.

631   Khaliq, Z.M., and Raman, I.M. (2005). Axonal propagation of simple and complex
632   spikes in cerebellar Purkinje neurons. The Journal of neuroscience : the official
633   journal of the Society for Neuroscience *25*, 454-463.

634   Khavandgar, S., Walter, J.T., Sageser, K., and Khodakhah, K. (2005). Kv1 channels
635   selectively prevent dendritic hyperexcitability in rat Purkinje cells. The Journal of
636   physiology *569*, 545-557.

637   Kitamura, K., and Hausser, M. (2011). Dendritic calcium signaling triggered by
638   spontaneous and sensory-evoked climbing fiber input to cerebellar Purkinje cells
639   in vivo. The Journal of neuroscience : the official journal of the Society for
640   Neuroscience *31*, 10847-10858.

641   Llinas, R., and Sugimori, M. (1980). Electrophysiological properties of in vitro
642   Purkinje cell dendrites in mammalian cerebellar slices. The Journal of physiology
643   *305*, 197-213.

644   Mano, N. (1970). Changes of simple and complex spike activity of cerebellar
645   purkinje cells with sleep and waking. Science *170*, 1325-1327.

646   Marr, D. (1969). A theory of cerebellar cortex. The Journal of physiology *202*, 437-
647   470.

648   Martina, M., Metz, A.E., and Bean, B.P. (2007). Voltage-dependent potassium
649   currents during fast spikes of rat cerebellar Purkinje neurons: inhibition by BDS-I
650   toxin. Journal of neurophysiology *97*, 563-571.

651   Martina, M., Yao, G.L., and Bean, B.P. (2003). Properties and functional role of
652   voltage-dependent potassium channels in dendrites of rat cerebellar Purkinje
653   neurons. The Journal of neuroscience : the official journal of the Society for
654   Neuroscience *23*, 5698-5707.

655   Maruta, J., Hensbroek, R.A., and Simpson, J.I. (2007). Intraburst and interburst
656   signaling by climbing fibers. The Journal of neuroscience : the official journal of
657   the Society for Neuroscience *27*, 11263-11270.

Masoli, S., Solinas, S., and D'Angelo, E. (2015). Action potential processing in a detailed Purkinje cell model reveals a critical role for axonal compartmentalization. Front Cell Neurosci *9*, 47.

Mathy, A., Ho, S.S., Davie, J.T., Duguid, I.C., Clark, B.A., and Hausser, M. (2009). Encoding of oscillations by axonal bursts in inferior olive neurons. Neuron *62*, 388-399.

Monsivais, P., Clark, B.A., Roth, A., and Hausser, M. (2005). Determinants of action potential propagation in cerebellar Purkinje cell axons. The Journal of neuroscience : the official journal of the Society for Neuroscience *25*, 464-472.

Najafi, F., Giovannucci, A., Wang, S.S., and Medina, J.F. (2014). Coding of stimulus strength via analog calcium signals in Purkinje cell dendrites of awake mice. eLife *3*, e03663.

Ohtsuki, G., Piochon, C., Adelman, J.P., and Hansel, C. (2012). SK2 channel modulation contributes to compartment-specific dendritic plasticity in cerebellar Purkinje cells. Neuron *75*, 108-120.

Otsu, Y., Marcaggi, P., Feltz, A., Isope, P., Kollo, M., Nusser, Z., Mathieu, B., Kano, M., Tsujita, M., Sakimura, K.*, et al.* (2014). Activity-dependent gating of calcium spikes by A-type K+ channels controls climbing fiber signaling in Purkinje cell dendrites. Neuron *84*, 137-151.

Palmer, L.M., Clark, B.A., Grundemann, J., Roth, A., Stuart, G.J., and Hausser, M. (2010). Initiation of simple and complex spikes in cerebellar Purkinje cells. The Journal of physiology *588*, 1709-1717.

Piochon, C., Titley, H.K., Simmons, D.H., Grasselli, G., Elgersma, Y., and Hansel, C. (2016). Calcium threshold shift enables frequency-independent control of plasticity by an instructive signal. Proceedings of the National Academy of Sciences of the United States of America *113*, 13221-13226.

Rancz, E.A., and Hausser, M. (2010). Dendritic spikes mediate negative synaptic gain control in cerebellar Purkinje cells. Proceedings of the National Academy of Sciences of the United States of America *107*, 22284-22289.

Rokni, D., Tal, Z., Byk, H., and Yarom, Y. (2009). Regularity, variability and bi-stability in the activity of cerebellar purkinje cells. Front Cell Neurosci *3*, 12.

Roth, A., and Hausser, M. (2001). Compartmental models of rat cerebellar Purkinje cells based on simultaneous somatic and dendritic patch-clamp recordings. The Journal of physiology *535*, 445-472.

Schmolesky, M.T., Weber, J.T., De Zeeuw, C.I., and Hansel, C. (2002). The making of a complex spike: ionic composition and plasticity. Annals of the New York Academy of Sciences *978*, 359-390.

Steuber, V., Mittmann, W., Hoebeek, F.E., Silver, R.A., De Zeeuw, C.I., Hausser, M., and De Schutter, E. (2007). Cerebellar LTD and pattern recognition by Purkinje cells. Neuron *54*, 121-136.

Stuart, G., and Hausser, M. (1994). Initiation and spread of sodium action potentials in cerebellar Purkinje cells. Neuron *13*, 703-712.

Swensen, A.M., and Bean, B.P. (2003). Ionic mechanisms of burst firing in dissociated Purkinje neurons. The Journal of neuroscience : the official journal of the Society for Neuroscience *23*, 9650-9663.

Vetter, P., Roth, A., and Hausser, M. (2001). Propagation of action potentials in dendrites depends on dendritic morphology. Journal of neurophysiology *85*, 926-937.

706 Wang, S.S., Denk, W., and Hausser, M. (2000). Coincidence detection in single
707 dendritic spines mediated by calcium release. Nature neuroscience *3*, 1266-1273.
708 Warnaar, P., Couto, J., Negrello, M., Junker, M., Smilgin, A., Ignashchenkova, A.,
709 Giugliano, M., Thier, P., and De Schutter, E. (2015). Duration of Purkinje cell
710 complex spikes increases with their firing frequency. Front Cell Neurosci *9*.
711 Wilms, C.D., and Hausser, M. (2015). Reading out a spatiotemporal population
712 code by imaging neighbouring parallel fibre axons in vivo. Nature communications
713 *6*, 6464.
714 Womack, M.D., and Khodakhah, K. (2003). Somatic and dendritic small-
715 conductance calcium-activated potassium channels regulate the output of
716 cerebellar Purkinje neurons. The Journal of neuroscience : the official journal of
717 the Society for Neuroscience *23*, 2600-2607.
718 Yang, Y., and Lisberger, S.G. (2014). Purkinje-cell plasticity and cerebellar motor
719 learning are graded by complex-spike duration. Nature *510*, 529-532.
720 Zagha, E., Manita, S., Ross, W.N., and Rudy, B. (2010). Dendritic Kv3.3 potassium
721 channels in cerebellar purkinje cells regulate generation and spatial dynamics of
722 dendritic Ca2+ spikes. Journal of neurophysiology *103*, 3516-3525.
723

724 # Supplementary Information

725

726 ## **Supplementary Figures**
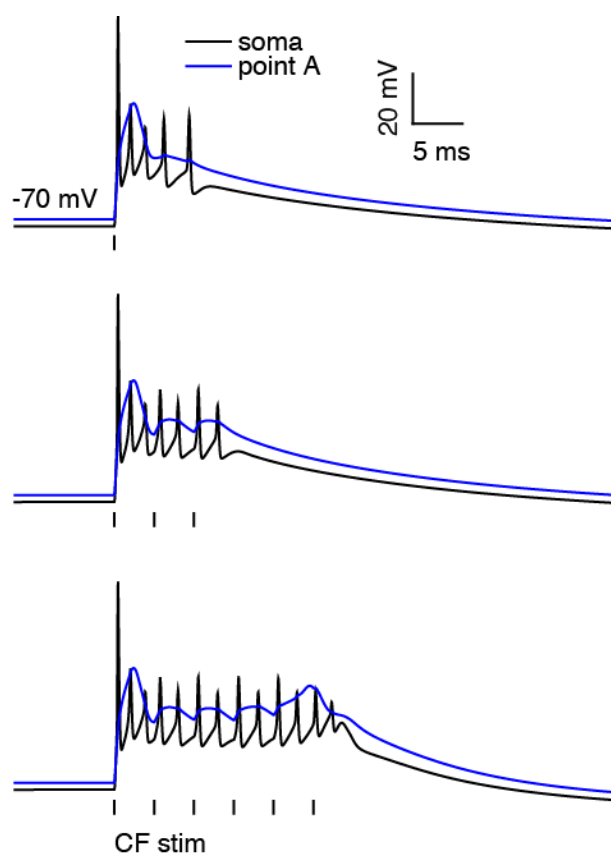
727
728 **Figure S1. PC responses to CF bursts. Related to Figure 1.**
729 We reproduced the experiment by Mathy et al. (2009). Example somatic and dendritic responses to CF
730 burst with 1 (top), 3 (middle) and 6 spikes (bottom) in the CF burst. The simulated instantaneous CF
731 bursting frequency is 250 Hz close to the experimentally reported ~ 273 Hz.
732
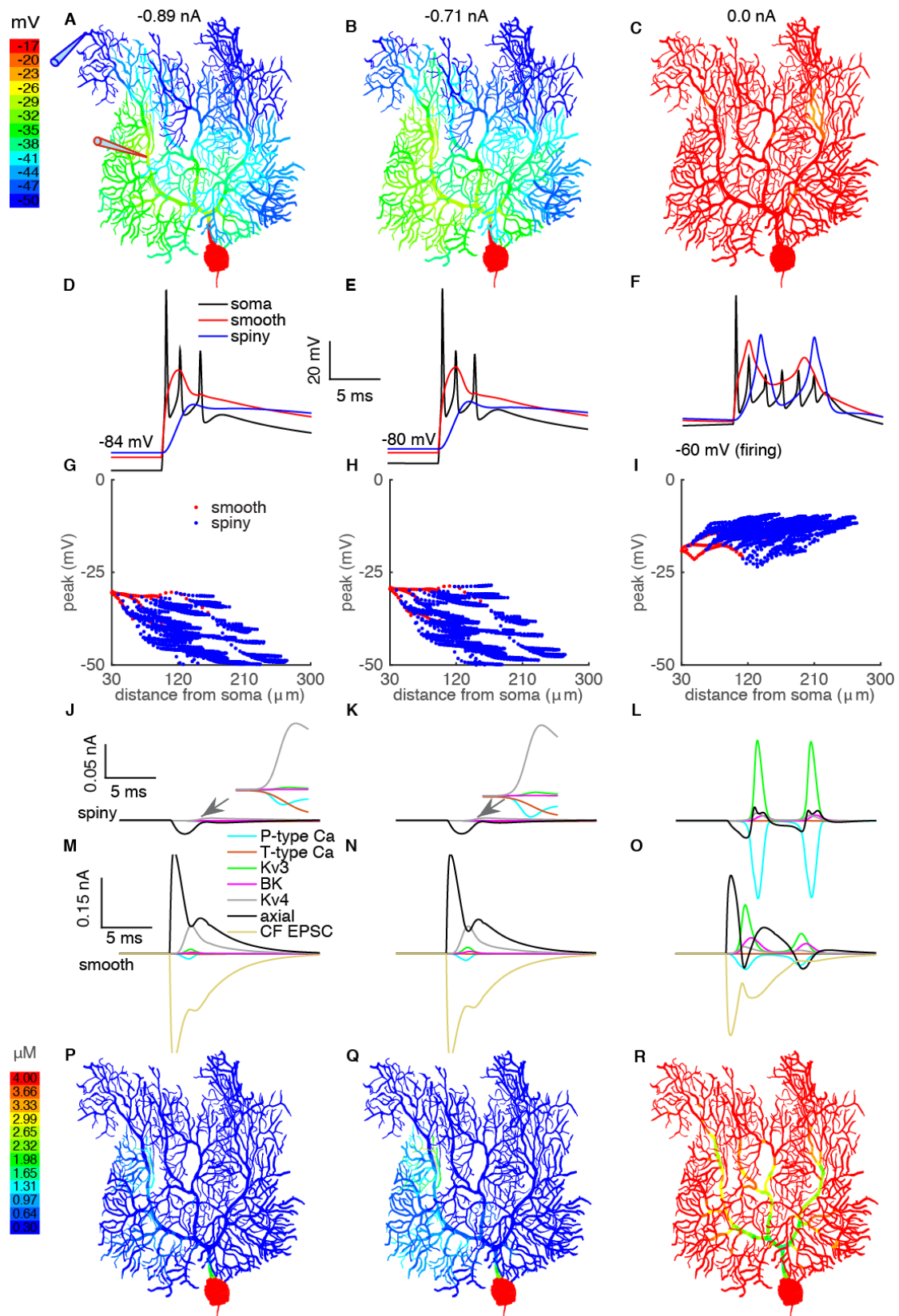
733
734 **Figure S2. Voltage states regulate CF-evoked dendritic spike generation and propagation. Related**
735 **to Figure 3.**
736 From left to right column, the holding potentials are -84 mV, -80 mV and -60 mV respectively. **A-C.**
737 Color-coded voltage responses. **D-F.** Somatic CSs, voltage responses on the smooth dendrite and spiny
738 dendrite. **G-I.** Distance-dependent propagation of voltage responses. **J-L** and **M-O** show ionic currents
739 in the spiny dendrite and smooth dendrite respectively. The surface areas of the segments chosen at the

22

740 smooth dendrite and spiny dendrite are 64 μm^2 and 23 μm^2 respectively. **P-R.** Color-coded Ca^{2+}
741 concentrations.
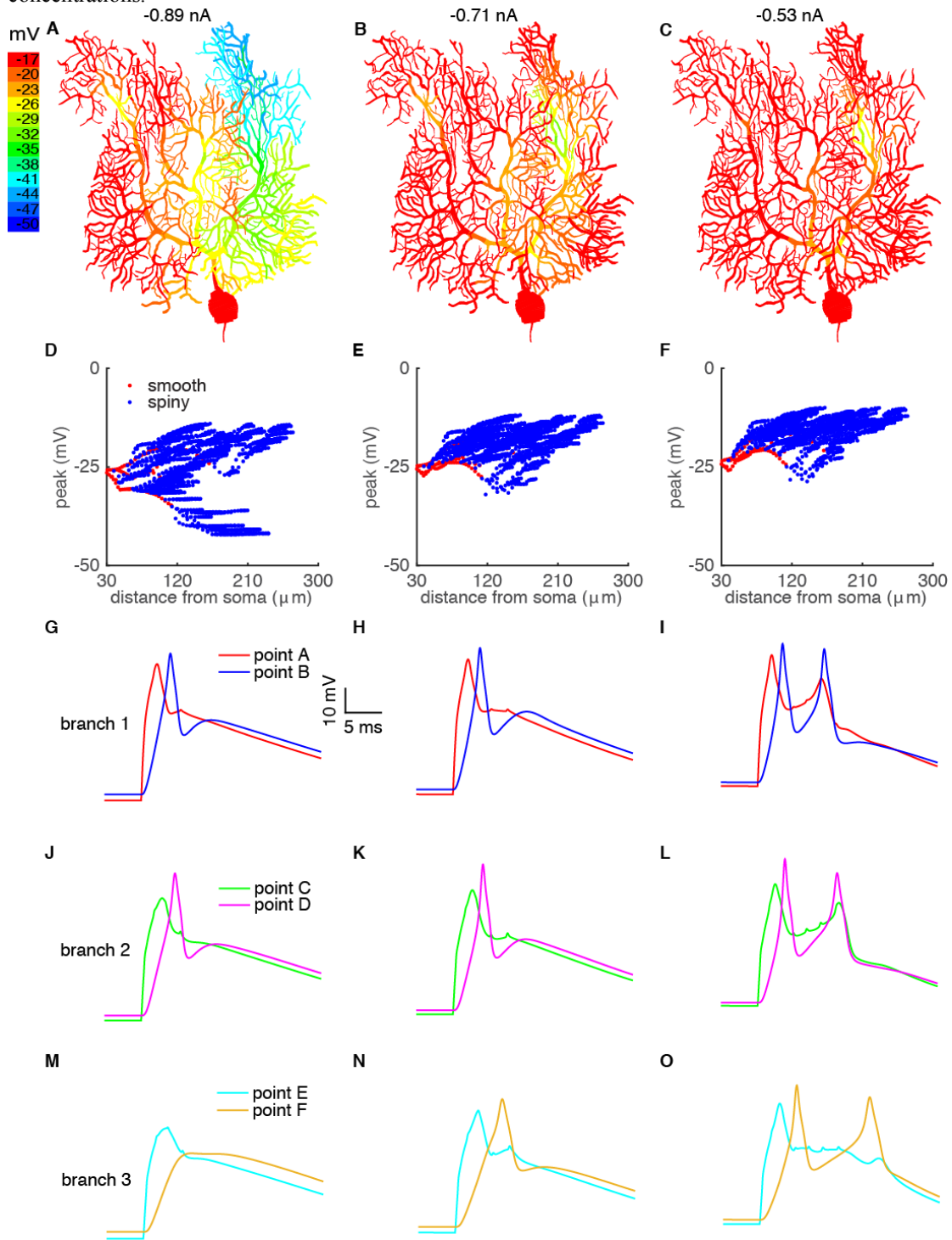
742
743
744 **Figure S3. locking Kv4 current facilitates dendritic spike generation and propagation and makes**
745 **dendritic excitability more homogeneous. Related to Figure 3 and Figure 4.**
746 Dendritic responses to holding currents of -0.89 nA, -0.71 nA and -0.53 nA are shown from left to right.
747 Color-coded voltage response, distance-dependent propagation of voltage response, and voltage
748 responses (EPSP or spike) at different branches are shown from top to bottom. The definition of recorded
749 dendritic sites is the same as in Fig. 2.
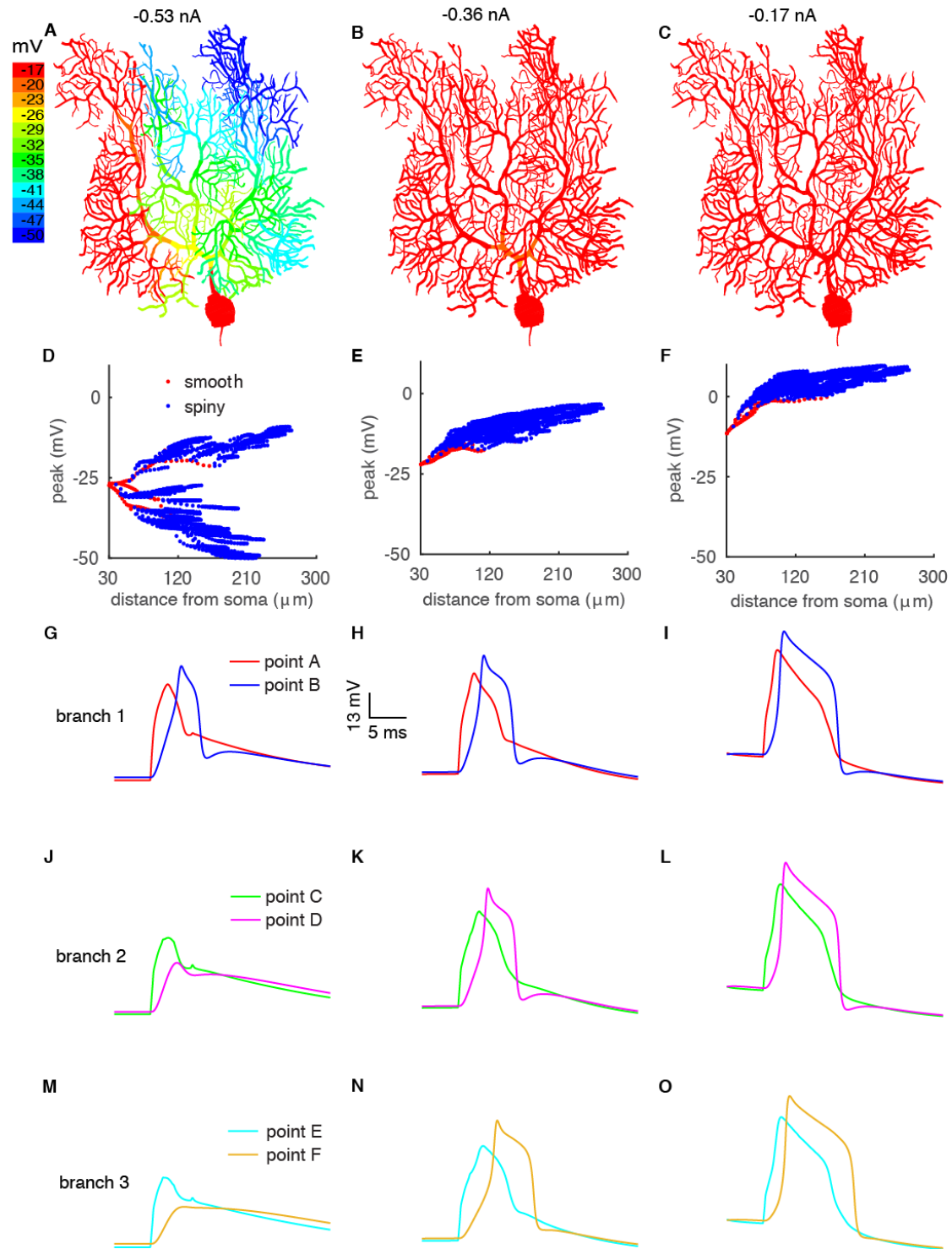
Fig S4. Blocking Kv3 current facilitates the propagation of dendritic spikes by increasing their durations. Related to Figure 3.
Dendritic responses with holding currents of -0.53 nA, -0.36 nA and -0.17 nA are shown from left to right. Color-coded voltage response, distance-dependent propagation of voltage response, and voltage responses (EPSP or spike) at different branches are shown from top to bottom. Notice the broader dendritic spikes (**G-O**) with an overshoot amplitude (dendritic peak is above 0 mV in **F**). The definition of recorded dendritic sites is the same as in Fig. 2.
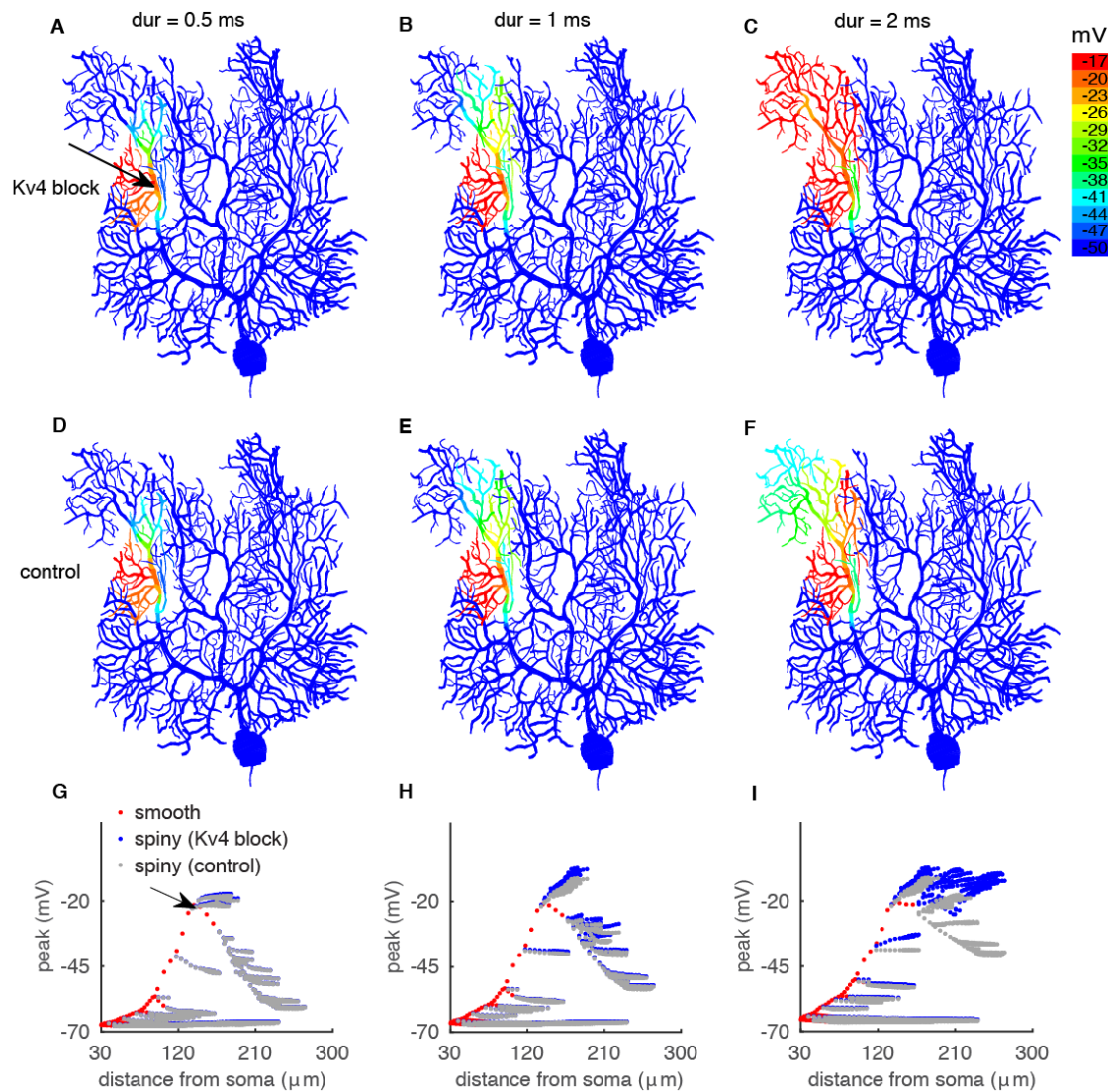
Fig S5. Broadening of dendritic spikes facilitates their propagation. Related to Figure 3.
We exerted square wave voltage clamps (peak is -20 mV, similar with dendritic spikes) with varying durations at the indicated sites of the smooth dendrite to explore propagation efficiency. The duration increases from 0.5 ms to 2 ms from **A** to **C** (Kv4 block) and **D** to **F** (control). The distance-dependent propagation of this signal is shown in **G-I** to reflect the relative contribution of impedance mismatch and Kv4 current on the decay of this signal. The clamped site is indicated in **G**. The PC is voltage clamped to -70 mV at the soma. Notice that Kv4 block did not affect the forward propagation to the soma of this signal.
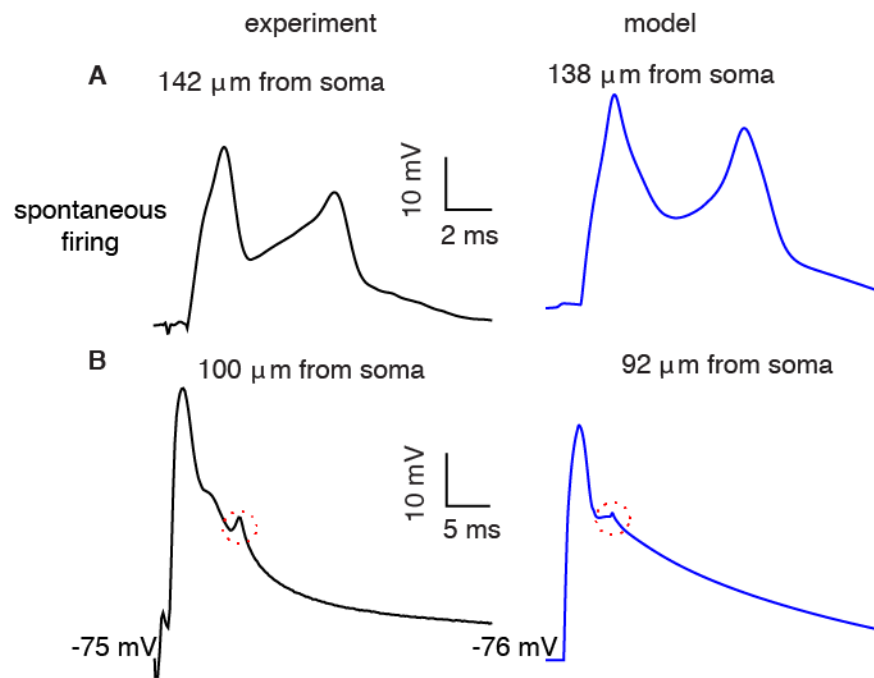
Figure S6. CF-evoked dendritic voltage response waveforms with different current injections (holding potentials). Related to Figure 3.
A. CF-evoked dendritic spikes with two spikelets in the experiment (left, reproduced from Fig. 5A of Davie et al. (2008)) and in the model (right). **B.** CF-evoked dendritic voltage responses in the experiment (left, data from Ohtsuki et al. (2012)) and in the model (right). The 'deflection' caused by a somatic Na$^+$ spikelet can be found on top of the dendritic response under this condition in both experimental recordings and in the model (circled in the figure).
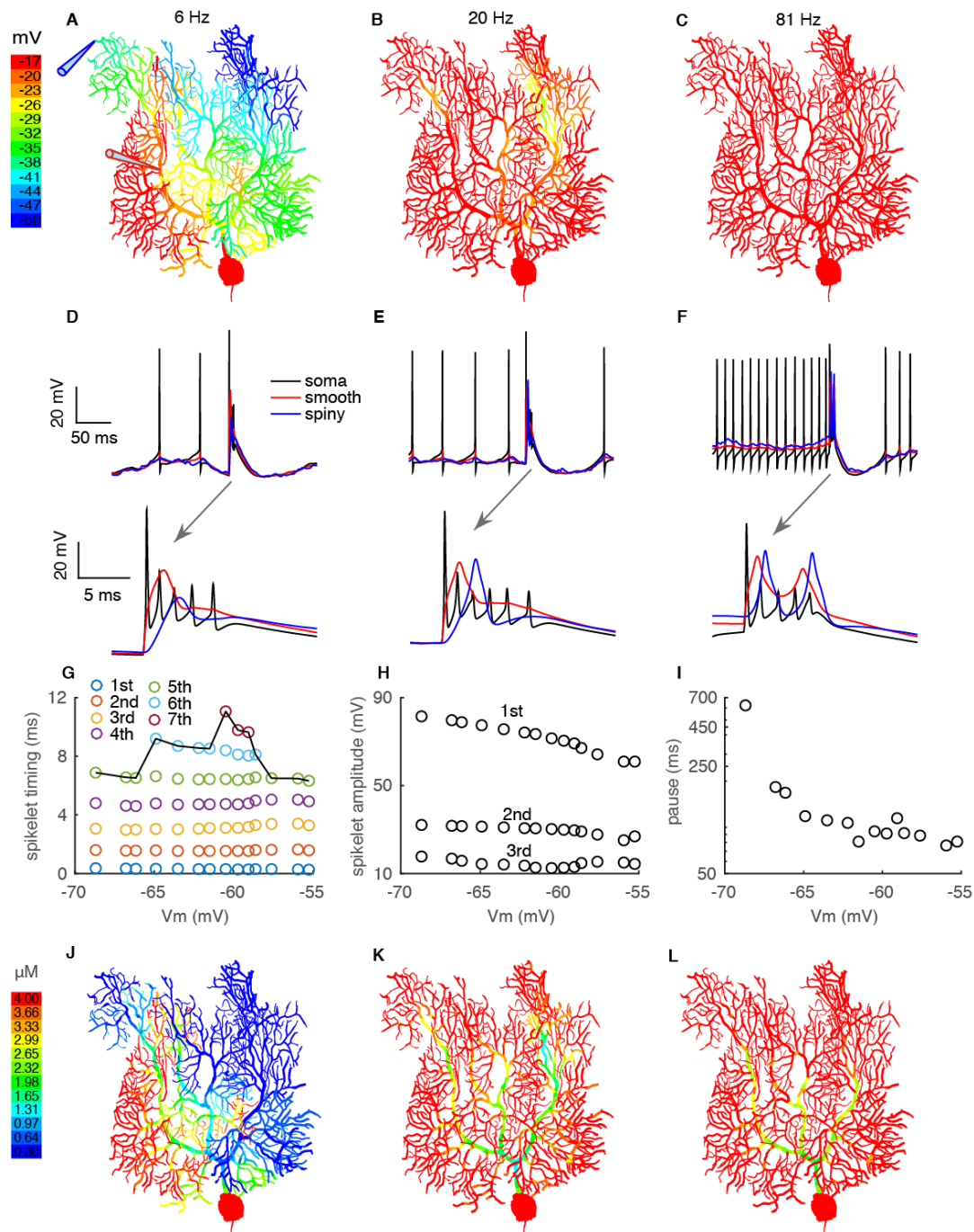
Figure S7. CF responses when the voltage states of the PC are manipulated by combined excitatory and inhibitory synaptic inputs. Related to Figure 5.
A-C show color-coded voltage responses with increasing SSFRs. **D-F** show the corresponding somatic and dendritic responses. CF responses at a higher time scale are shown in their bottom panels. **G** shows the effect of somatic voltage states on the CS spikelet numbers and durations. **H.** Effect of somatic voltage states on the amplitudes of the first 3 somatic spikelets. **I.** CF-evoked pause decreases with depolarization. **J-L** show color-coded Ca^{2+} concentrations with increasing SSFRs.
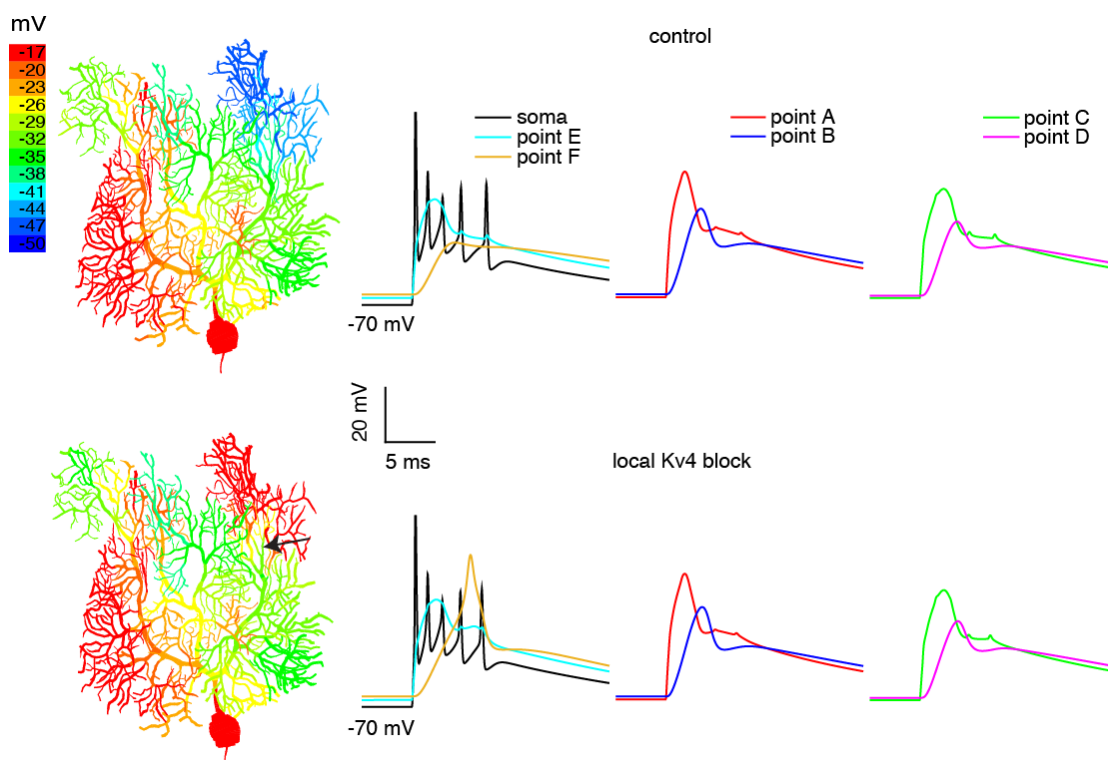
787
Figure S8. Local Kv4 block modulates dendritic responses in a spatially precise manner. Related to Figure 6.
In the child branchlet of the labeled dendritic section, Kv4 current is blocked (bottom panel). Only the dendritic responses located within the labeled branchlet (For example, Point F) are facilitated by the local Kv4 block. In other parts of the dendrite, dendritic responses are not affected. The definition of recorded dendritic sites is the same as in Fig. 2.

794
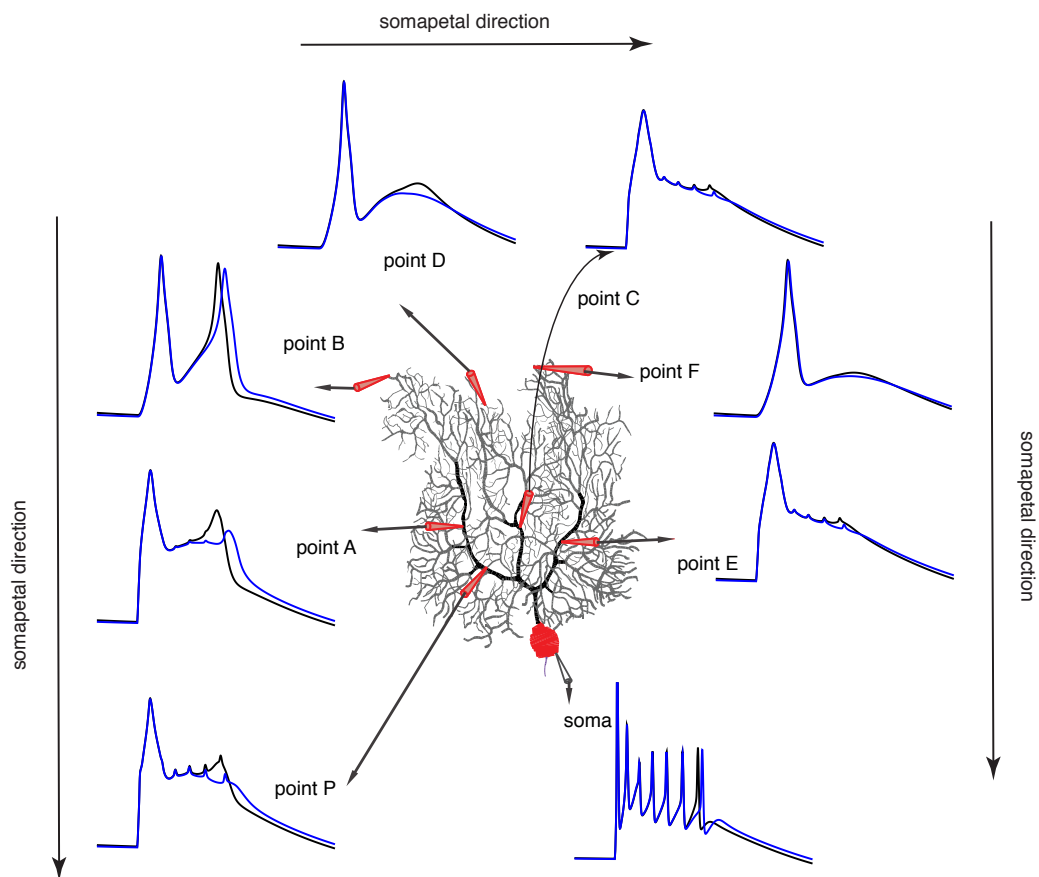
Figure S9. The dendritic spike measured on the proximal smooth dendrite can't reflect dendritic responses in the rest of the dendrite. This figure supports our results in Fig.5 and Discussion.
Here we reproduce the experiment by Davie et al. (2008). The holding current is -0.2 nA. The CF is activated at different phases of the somatic interspike interval to achieve a slight change of the dendritic membrane potential. In case I (blue traces), a secondary dendritic spikelet occurs at point B of the distal dendrite. However, at point A and P of the same branch (branch 1) closer to the soma, no secondary dendritic spikelets are triggered. With a slight depolarization of the dendrite in case II (black traces), secondary dendritic spikelets occur at both proximal sites (point A and point P) and at the distal site (point B).

804

Supplementary Experimental Procedures

Current equations and calcium handling

807   1) Na$^+$ current in the PC.

808   Na$^+$ current in the model is distributed in the AIS and soma. Na$^+$ current in the PC is
809   composed of 'transient', 'persistent' and 'resurgent' components. We started from the
810   previous model (Khaliq et al., 2003) and made slight changes (Narsg). In the soma, we
811   adjusted the reaction rates between the I1 - I5 states by right shifting 5 mV (Yan et al.,
812   2014): $\alpha = 150\, e^{(V-5)/20}$, $\beta = 3\, e^{(V-5)/-20}$. Other parameters are the same as the
813   original model. This adjustment mainly right-shifts the inactivation curve of this current
814   by ~ 2.5 mV. The inactivation curve of the modified model lies within measurements
815   (Raman and Bean, 2001; Yan et al., 2014). In the AIS, in addition to the above-
816   mentioned adjustment, we also adjusted deactivation rates between C1 - C5 to lower
817   the spike threshold in the AIS, as done by Colbert and Pan (2002). Therefore, $\beta = $
818    $3\, e^{(V+15)/-15}$ for reaction rates between C1 - C5. First, by this adjustment, the
819   contribution of AIS spikes to somatic spikes is closer to measured data (represented by
820   d^2V/dt^2 in Fig. 1D). Second, we removed the frequently failed recovery of simple spikes
821   after a complex spike when there is no obvious after-hyperpolarization following the
822   complex spike (although this can be observed in some experiments, data shared by Paul
823   Mathews from UCLA).
824   It is impossible to approximate Na$^+$ currents using a single model, given their multiple
825   components. In the original model (Khaliq et al., 2003), the persistent component is
826   tiny. Therefore, we incorporated an additional persistent Na$^+$ current model to
827   compensate (NaP). The steady state activation curve is from Carter et al. (2012), $m_{ss} = $
828    $1/(1 + e^{-(V+66)/5})$. The time constant is from Baker (2005), $\tau_m = 1/(\alpha_m + $
829    $\beta_m)$, $\alpha_m = 1/(\,17.235/(1+e^{(V+27.58)/-11.47})\,)$, $\beta_m = 1/(\,17.235/(1+e^{(V+86.2)/19.8})\,)$.
830   This persistent component helps to maintain spike firing during negative current
831   injections.

832   2) H-current in the PC

833   H-current (Ih) is distributed in the whole PC (Angelo et al., 2007). In our model, the
834   formulations are the same as the model formulations from Angelo et al. (2007), except
835   we shifted the activation curve to a more hyperpolarized direction by 6 mV to make
836   'sag' responses with different holding currents more comparable to experimental
837   recordings (Fig. 1G).

838   3) T-type Ca^{2+} current in the PC

839   T-type Ca^{2+} current is distributed in the AIS (Bender and Trussell, 2009), the smooth
840   dendrite and the spiny dendrite (Hildebrand et al., 2009; Otsu et al., 2014). The
841   formulation of this current is according to data from Otsu et al. (2014). $m_{ss} = 1/(1 + $
842    $e^{-(V-35.606)/4.7})$, $\tau_m = 1/(1.2757 + \alpha_m + \beta_m)$, $\alpha_m = -2.3199/(1 + $
843    $e^{(V+41.448)/-30.655})$, $\beta_m = 2.5712/(1 + e^{(V+21.7866)/-9.6306})$, $h_{ss} = 1/(1 + $
844    $e^{(V+81.718)/6.4635})$, $\tau_h = 1/(0.0076 + \alpha_h + \beta_h)$, $\alpha_h = 0.17746/(1 + $
845    $e^{(V+41.448)/-30.655})$, $\beta_h = 0.13402/(1 + e^{(V+94.836)/-5.5845})$. In the model, both BK
846   and SK2 don't sense Ca^{2+} influx from T-type Ca^{2+} channels.

847   4) P-type Ca^{2+} current in the PC

848   P-type Ca^{2+} current is distributed throughout the entire PC (Indriati et al., 2013). The
849   formulation of this current is according to the data from Benton and Raman (2009).

850     $m_{ss} = 1/(1 + e^{-(V-25.5)/4.113}), \tau_m = 0.2 + 0.7031 e^{-((V+25)/14)^2}$.

851   5) Ca^{2+} handling mechanism

852   In the dendrite, we used the formulation from Anwar et al. (2012) with 4 shells. In both
853   soma and AIS, we made BK channels sense Ca^{2+} signals closer to the membrane surface
854   (subspace) or Ca^{2+} channels by increasing the number of shells (Indriati et al., 2013).
855   In the AIS, we still used the formulation as in Anwar et al. (2012), but we increased the
856   number of shells to 10. In the soma, we used the fixed depth scheme for the outermost
857   shell and 20 shells in total to reduce the computational load (Anwar et al., 2014). We
858   also incorporated a sarcoplasmic endoplasmic reticulum Ca^{2+}ATPase (SERCA) pump
859   to reduce the spike-over-spike Ca^{2+} summation in AIS and soma. $J_{SERCA} = 0.1 *$
860     $vol(i) * Ca[i]/(Ca[i] + 0.0058(mM))$, $vol(i)$ means the volume of the i_{th} shell.
861     $Ca[i]$ means the free Ca^{2+} concentration of the i_{th} shell.

862   6) BK current in the PC

863   We used the same formulation from Anwar et al. (2012) as the fast (or IBTX-sensitive)
864   component of the BK current (Benton et al., 2013). We also incorporated the slow (or
865   IBTX-insensitive) component of BK current (Benton et al., 2013) from Jaffe et al.
866   (2011). The formulation of their type II model was used. The fast component is
867   distributed in the whole PC and the slow component is only distributed in the soma and
868   the AIS.

869   7) SK2 current in the PC

870   SK2 current is distributed in the whole PC (Belmeguenai et al., 2010; Swensen and
871   Bean, 2003). We used the formulation from Solinas et al. (2007) according to the data
872   by Hirschberg et al. (1998).

873   8) Kv3 current in the PC

874   KV3 current is distributed in the whole PC (Martina et al., 2003). The formulation is
875   from Akemann et al. (2009) according to the data from Martina et al. (2007). In our
876   model, the steady state activation curve is left shifted by 4 mV with $V_{0.5} \approx 2$ mV, which
877   is still within the experimental range (Martina et al., 2007; Martina et al., 2003; Zagha
878   et al., 2010).

879   9) Kv4 current in the PC

880   In our model, Kv4 current has both fast and slow inactivation components and is
881   distributed in the smooth and the spiny dendrites (Otsu et al., 2014). We took the steady
882   state activation curve from Gunay et al. (2008). The inactivation curve and time
883   constants are according to experimental data of Stéphane Dieudonné. $m_{ss} = 1/(1 +$
884     $e^{(V+49)/-12.5})$, $\tau_m = 1/(\alpha_m + \beta_m)$, $\alpha_m = 0.1342/(1 + e^{(V+60)/32.19976})$, $\beta_m =$
885     $0.15743/(1 + e^{(V+57)/37.51346})$, $h_{ss} = 1/(1 + e^{(V+75.30348)/6.06329})$, $\tau_{hf} = 1/$
886     $(\alpha_{hf} + \beta_{hf})$, $\alpha_{hf} = 0.01342/(1 + e^{(V+60)/7.86476})$, $\beta_{hf} = 0.04477/(1 +$
887     $e^{(V+54)/-11.6315})$, $\tau_{hs} = 100$.

888   10) Kv1 current in the PC

889   In our model, Kv1 is distributed in the dendrite (Khavandgar et al., 2005). The
890   formulation is from Akemann and Knopfel (2006). We added an inactivation gate,

891 according to data from Otsu et al. (2014). $h_{ss} = 1/(1 + e^{(V+66.16)/6.1881})$. Due to the
892 slow inactivation process, the inactivation time constant was set to be 1000 ms.

Parameter tuning

894 The model was hand-tuned because extensive preceding efforts using automatic
895 parameter searching did not achieve good results (Achard and De Schutter, 2006; Van
896 Geit et al., 2007). Due to technical limitations, we can only get simultaneous somatic
897 and dendritic patch-clamp recordings (single dendritic site) to constrain the model in
898 most cases. However, it has been demonstrated that data recorded from just two
899 locations in the same L5 pyramidal neuron are insufficient to accurately constrain a
900 compartmental model (Keren et al., 2005). For the PC, we were able to get good F-I
901 curves and 'sag' responses with automated search methods, but the dendrite model
902 could not generate physiologic responses. This is because we don't have sufficient data
903 to constrain the active properties of the dendrite and the interaction between soma and
904 dendrite by automatic parameter searching. Therefore, we decided to use hand-tuning
905 instead, and we tried to incorporate as many experimental observations as possible into
906 the model. After repeated modification over a period of more than two years, we
907 achieved the present model.

908 1) Currents in the soma

909 The Na$^+$ current profile nearly coincides with the total net ionic current during the
910 depolarization phase of dissociated PC AP-clamp recordings (Carter and Bean, 2009).
911 The total net ionic current is calculated by –C*dV/dt, where C is the cell capacitance
912 and dV/dt is the time derivative of the voltage. The results of Carter and Bean suggest
913 that Na$^+$ current is nearly the sole current supporting the depolarization and K$^+$ currents
914 are not activated during the depolarization phase (as illustrated in Fig. 2 of their paper).
915 This also agrees with the high activation threshold of K$^+$ currents in the PC (Martina et
916 al., 2007). This finding provided an opportunity to firmly constrain the somatic ionic
917 currents. The measured peak Na$^+$ current amplitude is 12.5 nA in dissociated mouse
918 PCs with a capacitance of 12 pF, but the ratio of current/capacitance in the soma may
919 be underestimated due to the possible remaining stump of the dendritic tree. In our
920 model, we have a peak somatic Na$^+$ current of 17 nA relative to a capacitance of 10.5
921 pF in the soma. Then we get the conductance density of somatic Kv3 current by
922 constraining the spike half-amplitude duration (0.15 ms) close to experimental
923 measurements (0.17 ms, we also gave consideration to the spike duration in the intact
924 PC as shown in Fig. 1B). The high activation threshold of the Kv3 current makes it
925 active mainly during the repolarization phase (Carter and Bean, 2009) and constrains
926 the spike duration (Martina et al., 2007). Subsequently, we constrained the conductance
927 density of P-type Ca^{2+} current and BK current to have an AHP (-77 mV) comparable
928 to the recorded (-82 mV, still we also considered the AHP in the intact PC ~ -70 mV).
929 The conductance density of P-type Ca^{2+} is constrained to be the same as that in the
930 smooth dendrite. Then only SK2 and Ih remained unconstrained for the somatic ionic
931 currents. We initially assigned tentative conductance density values for these two
932 currents to develop a firing somata model (like the previous Kaliq-Raman model
933 (Khaliq et al., 2003)). To reflect the negligible role of Ih in dissociated PC firing
934 (Raman and Bean, 1999), the conductance density of Ih is half of that in smooth
935 dendrite. In the intact PC, the conductance density of somatic SK2 current is adjusted
936 to get a F-I curve close to the experimental measurements (Fig. 1G). The persistent
937 component of Na$^+$ current is constrained so that the intact PC still fires with -0.17 nA

32

938 somatic holding current, but it stops firing when the current amplitude changes to -0.36
939 nA.

940 2) Currents in the AIS

941 We constrained ionic currents in the AIS to make the model behave like experimental
942 data in two aspects: the axosomatic delay of the simple spike (Fig. 1B) and the second
943 derivative of the simple spike (Fig. 1D). The first reflects how the spike in the AIS
944 precedes the somatic spike and the second reflects the contribution of the spike in the
945 AIS to the somatic spike. We assumed the conductance densities of Ih in AIS are the
946 same as in soma.

947 3) Currents in the dendrite

948 Due to the limited quantitative data, ionic currents in the dendrite are more difficult to
949 constrain compared with somatic currents. We first constrained the P-type Ca^{2+} current
950 in the dendrite. In the spiny dendrite, Ca^{2+} influx during one dendritic spikelet is 1.3e-
951 14 $C/\mu m^3$ in our model, which is close to the experimentally estimated 1.1e-14 $C/\mu m^3$
952 (Otsu et al., 2014). The CF-evoked Ca^{2+} influx increases with distance from soma when
953 a Ca^{2+}-supported dendritic spike occurs (Kitamura and Hausser, 2011; Otsu et al., 2014).
954 Therefore, in the smooth dendrite, the current density was constrained to have a calcium
955 influx ratio (smooth dendrite relative to the spiny dendrite at same membrane surface
956 area) of 0.36. The conductance densities of P-type Ca^{2+} current are further supported
957 by the time to peak of the first dendritic spikelet being ~ 1.5 ms in the smooth dendrite
958 (Davie et al., 2008; Kitamura and Hausser, 2011). Conductance densities of Kv4 current
959 are assumed to be homogeneously distributed and then repeatedly adjusted to make this
960 current able to 'brake' the dendritic spikes at low voltage ranges. We distributed more
961 T-type Ca^{2+} channels (Hildebrand et al., 2009) in the spiny dendrite given they are
962 preferentially distributed on spines. This current helps to offset the window current of
963 Kv4 current to maintain the dendritic interspike interval membrane potential. We
964 distributed larger conductance densities of BK current on the smooth dendrite
965 compared to on spiny dendrite, given the BK channel clusters are mainly distributed on
966 the soma and smooth dendrite (Kaufmann et al., 2010). BK current contributes to
967 reasonable AHP after complex spikes as found in Davie et al. (2008). Ih is constrained
968 to get a 'sag' response close to the experimental recordings (Fig. 1G). Kv1 and SK2
969 help to regulate dendritic excitability to stop the occurrence of Na^+-Ca^{2+} bursting at low
970 current injections. In our model, as with most cell recordings in rat PCs, Na^+-Ca^{2+} bursts
971 begin to occur with 1.25 nA somatic current injection. In addition, this dendrite model
972 can replicate the distance-dependent decay of the simple spike amplitude (Fig. 1E), the
973 regulatory role of K^+ currents in voltage-dependent dendritic spike generation and
974 propagation (Fig. 3, S2-S4, S7), the dendritic voltage response waveforms at different
975 conditions (Fig. S6), and peak dendritic voltage response propagation with distance
976 from the soma at specific condition (Fig. 3G).

977

978 **Current conductance densities in different parts of the PC model**

979

Currents (nS/cm^2)	AIS	soma	smooth dendrite	spiny dendrite
Narsg	0.56	0.0317	0	0
NaP	0.0023	1.4e-4	0	0
Ih	1.08e-4	1.08e-4	2.16e-4	3.24e-4
T- type Ca^{2+}	1.28e-4	0	2.7e-5	1.08e-4

33

P-type Ca^{2+}	1.05	1.9e-4	1.9e-4	7.6e-4
BKfast	6	0.8736	0.21	0.0448
BKslow	1.05	0.3	0	0
SK2	0.0278	0.0075	2.16e-4	3.6e-4
Kv3	115	1.8	0.1512	0.2268
Kv4	0	0	0.015	0.015
Kv1	0	0	0.002	0.001

Supplementary References

Achard, P., and De Schutter, E. (2006). Complex parameter landscape for a complex neuron model. PLoS computational biology *2*, e94.

Akemann, W., and Knopfel, T. (2006). Interaction of Kv3 potassium channels and resurgent sodium current influences the rate of spontaneous firing of Purkinje neurons. The Journal of neuroscience : the official journal of the Society for Neuroscience *26*, 4602-4612.

Akemann, W., Lundby, A., Mutoh, H., and Knopfel, T. (2009). Effect of voltage sensitive fluorescent proteins on neuronal excitability. Biophysical journal *96*, 3959-3976.

Angelo, K., London, M., Christensen, S.R., and Hausser, M. (2007). Local and global effects of I(h) distribution in dendrites of mammalian neurons. The Journal of neuroscience : the official journal of the Society for Neuroscience *27*, 8643-8653.

Anwar, H., Hong, S., and De Schutter, E. (2012). Controlling Ca2+-activated K+ channels with models of Ca2+ buffering in Purkinje cells. Cerebellum *11*, 681-693.

Anwar, H., Roome, C.J., Nedelescu, H., Chen, W., Kuhn, B., and De Schutter, E. (2014). Dendritic diameters affect the spatial variability of intracellular calcium dynamics in computer models. Front Cell Neurosci *8*, 168.

Baker, M.D. (2005). Protein kinase C mediates up-regulation of tetrodotoxin-resistant, persistent Na+ current in rat and mouse sensory neurones. The Journal of physiology *567*, 851-867.

Belmeguenai, A., Hosy, E., Bengtsson, F., Pedroarena, C.M., Piochon, C., Teuling, E., He, Q., Ohtsuki, G., De Jeu, M.T., Elgersma, Y., *et al.* (2010). Intrinsic plasticity complements long-term potentiation in parallel fiber input gain control in cerebellar Purkinje cells. The Journal of neuroscience : the official journal of the Society for Neuroscience *30*, 13630-13643.

Bender, K.J., and Trussell, L.O. (2009). Axon initial segment Ca2+ channels influence action potential generation and timing. Neuron *61*, 259-271.

Benton, M.D., Lewis, A.H., Bant, J.S., and Raman, I.M. (2013). Iberiotoxin-sensitive and -insensitive BK currents in Purkinje neuron somata. Journal of neurophysiology *109*, 2528-2541.

Benton, M.D., and Raman, I.M. (2009). Stabilization of Ca current in Purkinje neurons during high-frequency firing by a balance of Ca-dependent facilitation and inactivation. Channels *3*, 393-401.

Carter, B.C., and Bean, B.P. (2009). Sodium entry during action potentials of mammalian neurons: incomplete inactivation and reduced metabolic efficiency in fast-spiking neurons. Neuron *64*, 898-909.

1020 Carter, B.C., Giessel, A.J., Sabatini, B.L., and Bean, B.P. (2012). Transient Sodium
1021 Current at Subthreshold Voltages: Activation by EPSP Waveforms. Neuron *75*,
1022 1081-1093.
1023 Colbert, C.M., and Pan, E. (2002). Ion channel properties underlying axonal action
1024 potential initiation in pyramidal neurons. Nature neuroscience *5*, 533-538.
1025 Davie, J.T., Clark, B.A., and Hausser, M. (2008). The origin of the complex spike in
1026 cerebellar Purkinje cells. The Journal of neuroscience : the official journal of the
1027 Society for Neuroscience *28*, 7599-7609.
1028 Gunay, C., Edgerton, J.R., and Jaeger, D. (2008). Channel density distributions
1029 explain spiking variability in the globus pallidus: a combined physiology and
1030 computer simulation database approach. The Journal of neuroscience : the official
1031 journal of the Society for Neuroscience *28*, 7476-7491.
1032 Hildebrand, M.E., Isope, P., Miyazaki, T., Nakaya, T., Garcia, E., Feltz, A., Schneider,
1033 T., Hescheler, J., Kano, M., Sakimura, K., *et al.* (2009). Functional Coupling between
1034 mGluR1 and Ca(v)3.1 T-Type Calcium Channels Contributes to Parallel Fiber-
1035 Induced Fast Calcium Signaling within Purkinje Cell Dendritic Spines. Journal of
1036 Neuroscience *29*, 9668-9682.
1037 Hirschberg, B., Maylie, J., Adelman, J.P., and Marrion, N.V. (1998). Gating of
1038 recombinant small-conductance Ca-activated K+ channels by calcium. The Journal
1039 of general physiology *111*, 565-581.
1040 Indriati, D.W., Kamasawa, N., Matsui, K., Meredith, A.L., Watanabe, M., and
1041 Shigemoto, R. (2013). Quantitative localization of Cav2.1 (P/Q-type) voltage-
1042 dependent calcium channels in Purkinje cells: somatodendritic gradient and
1043 distinct somatic coclustering with calcium-activated potassium channels. The
1044 Journal of neuroscience : the official journal of the Society for Neuroscience *33*,
1045 3668-3678.
1046 Jaffe, D.B., Wang, B., and Brenner, R. (2011). Shaping of action potentials by type I
1047 and type II large-conductance Ca(2)+-activated K+ channels. Neuroscience *192*,
1048 205-218.
1049 Kaufmann, W.A., Kasugai, Y., Ferraguti, F., and Storm, J.F. (2010). Two distinct
1050 pools of large-conductance calcium-activated potassium channels in the somatic
1051 plasma membrane of central principal neurons. Neuroscience *169*, 974-986.
1052 Keren, N., Peled, N., and Korngreen, A. (2005). Constraining compartmental
1053 models using multiple voltage recordings and genetic algorithms. Journal of
1054 neurophysiology *94*, 3730-3742.
1055 Khaliq, Z.M., Gouwens, N.W., and Raman, I.M. (2003). The contribution of
1056 resurgent sodium current to high-frequency firing in Purkinje neurons: an
1057 experimental and modeling study. The Journal of neuroscience : the official journal
1058 of the Society for Neuroscience *23*, 4899-4912.
1059 Khavandgar, S., Walter, J.T., Sageser, K., and Khodakhah, K. (2005). Kv1 channels
1060 selectively prevent dendritic hyperexcitability in rat Purkinje cells. The Journal of
1061 physiology *569*, 545-557.
1062 Kitamura, K., and Hausser, M. (2011). Dendritic calcium signaling triggered by
1063 spontaneous and sensory-evoked climbing fiber input to cerebellar Purkinje cells
1064 in vivo. The Journal of neuroscience : the official journal of the Society for
1065 Neuroscience *31*, 10847-10858.
1066 Martina, M., Metz, A.E., and Bean, B.P. (2007). Voltage-dependent potassium
1067 currents during fast spikes of rat cerebellar Purkinje neurons: inhibition by BDS-I
1068 toxin. Journal of neurophysiology *97*, 563-571.

1069 Martina, M., Yao, G.L., and Bean, B.P. (2003). Properties and functional role of
1070 voltage-dependent potassium channels in dendrites of rat cerebellar Purkinje
1071 neurons. The Journal of neuroscience : the official journal of the Society for
1072 Neuroscience *23*, 5698-5707.
1073 Otsu, Y., Marcaggi, P., Feltz, A., Isope, P., Kollo, M., Nusser, Z., Mathieu, B., Kano, M.,
1074 Tsujita, M., Sakimura, K.*, et al.* (2014). Activity-dependent gating of calcium spikes
1075 by A-type K+ channels controls climbing fiber signaling in Purkinje cell dendrites.
1076 Neuron *84*, 137-151.
1077 Raman, I.M., and Bean, B.P. (1999). Ionic currents underlying spontaneous action
1078 potentials in isolated cerebellar Purkinje neurons. The Journal of neuroscience :
1079 the official journal of the Society for Neuroscience *19*, 1663-1674.
1080 Raman, I.M., and Bean, B.P. (2001). Inactivation and recovery of sodium currents
1081 in cerebellar Purkinje neurons: evidence for two mechanisms. Biophysical journal
1082 *80*, 729-737.
1083 Solinas, S., Forti, L., Cesana, E., Mapelli, J., De Schutter, E., and D'Angelo, E. (2007).
1084 Computational reconstruction of pacemaking and intrinsic electroresponsiveness
1085 in cerebellar Golgi cells. Front Cell Neurosci *1*, 2.
1086 Swensen, A.M., and Bean, B.P. (2003). Ionic mechanisms of burst firing in
1087 dissociated Purkinje neurons. The Journal of neuroscience : the official journal of
1088 the Society for Neuroscience *23*, 9650-9663.
1089 Van Geit, W., Achard, P., and De Schutter, E. (2007). Neurofitter: a parameter
1090 tuning package for a wide range of electrophysiological neuron models. Frontiers
1091 in neuroinformatics *1*, 1.
1092 Yan, H., Pablo, J.L., Wang, C., and Pitt, G.S. (2014). FGF14 modulates resurgent
1093 sodium current in mouse cerebellar Purkinje neurons. eLife *3*, e04193.
1094 Zagha, E., Manita, S., Ross, W.N., and Rudy, B. (2010). Dendritic Kv3.3 potassium
1095 channels in cerebellar purkinje cells regulate generation and spatial dynamics of
1096 dendritic Ca2+ spikes. Journal of neurophysiology *103*, 3516-3525.
1097